Hybrid Wing-Body Aircraft Noise and Performance Assessment

by

Philip Andrew Weed

Bachelor of Science in Engineering, University of Michigan (2003)

Submitted to the Department of Aeronautics and Astronautics
in partial fulfillment of the requirements for the degree of

Master of Science in Aeronautics and Astronautics

at the

MASSACHUSETTS INSTITUTE OF TECHNOLOGY

June 2010

Author . . . .
Department of Aeronautics and Astronautics
May 21, 2010

Certified by . . . .
Zoltán S. Spakovszky
H. N. Slater Associate Professor
Thesis Supervisor

Accepted by . . . .
Eytan H. Modiano
Associate Professor of Aeronautics and Astronautics
Chair, Committee on Graduate Students

Hybrid Wing-Body Aircraft Noise and Performance Assessment

by

Philip Andrew Weed

Submitted to the Department of Aeronautics and Astronautics
on May 21, 2010, in partial fulfillment of the requirements for the degree of
Master of Science in Aeronautics and Astronautics

Abstract

Hybrid wing-body aircraft noise generation and boundary layer ingestion (BLI) performance trends with increased fan face Mach number inlet designs are investigated. The presented topics are in support of the NASA subsonic fixed wing project, which seeks to lower noise and increase performance by improving prediction methods and technologies. The aircraft configurations used for study are the N2A, using conventional podded engines, and the N2B, using an embedded propulsion system.

Preliminary FAR Part 36 noise certification assessments are completed using the NASA Aircraft Noise Prediction Program (ANOPP). The limitations of applying current ANOPP noise prediction methods to hybrid wing-body aircraft are investigated. Improvements are made to the landing gear and airfoil self-noise modules, while a diffraction integral method is implemented in a companion thesis to enhance noise shielding estimates. The N2A overall takeoff and landing noise estimate is found to be 5.3 EPNdB higher than the N+2 goal. The dominant noise sources are the fan rearward and jet on takeoff and the main landing gear and elevons on approach. A lower fan pressure ratio and advanced landing gear fairings are recommended to decrease N2A overall noise levels. The available engine noise estimation tools were inadequate to model the N2B distributed propulsion system and rectangular exhaust nozzle; therefore, overall N2B aircraft noise results are presented for reference only.

A simplified embedded propulsion system integration study is carried out to explore the N2B fan design space. A 2-D computational domain with contoured slip boundaries around the centerbody is used to replicate the effects of 3-D relief on the airframe and inlet aerodynamics. The domain includes the S-shaped inlet duct and is extended far downstream for a Trefftz plane power balance analysis to determine the propulsive power required for steady level flight. A fan actuator volume is included to couple the airframe external and the engine internal flows. Aircraft power savings, fan efficiency, and boundary layer thickness trends are examined to determine if increasing fan face Mach number improves system performance while mitigating the total pressure distortion risk of boundary layer ingestion. A fan face Mach number near 0.7 is found to increase aircraft power savings 12% relative to the baseline design and to reduce centerbody boundary layer kinetic energy thickness by 4.7%. In addition, power balances at lower fan pressure ratios as fan face Mach number increases suggesting that high-flow low pressure ratio fans are desirable for BLI.

Thesis Supervisor: Zoltán S. Spakovszky
Title: H. N. Slater Associate Professor

To my wife, Maja. There are no words to convey my gratitude for the encouragement, support, and sacrifice you have given me except . . . I love you.

Acknowledgments

I would like to thank my advisor Professor Spakovszky for his technical guidance throughout the research process and for pushing me to give my very best.

I am indebted to my GE colleagues for their support while completing my degree. My co-workers have been very accommodating of my work schedule and provided a great deal of encouragement along the way. I would also like to thank my GE ACE support group, Jon Kerner and Alex Narkaj.

This research would not have been possible without input from several people. Casey Burley and Jeff Burton at NASA provided ANOPP support, as well as, the engine cycle and noise data. Dr. Dimitri Papamoschou at the University of California Irvine contributed the jet noise and shielding data. Ron Kawai at Boeing provided the N2A and N2B flight trajectories and final aircraft configurations.

I am very proud to be a part of the GTL where the intellectual discussions and collaborative atmosphere greatly enhanced my educational experience. Thank you to Jeff Defoe for sharing his time and wealth of FLUENT knowledge. Most especially thank you to my research partner, Leo Ng, for his invaluable technical insight and friendship.

I would like to thank my parents, Jim and Beth, and my sisters, Laura and Michelle, for their continued love and support.

My degree was sponsored by the General Electric Company through the Advanced Courses in Engineering, under the supervision of Tyler Hooper and Ken Gould. Additional research funding was provided through NASA NRA NNH06ZEA001N Amendment 4 as a subcontract to Boeing Phantom Works in Huntington Beach California. I am extremely grateful for their support.

THIS PAGE INTENTIONALLY LEFT BLANK

Contents

List of Figures

List of Tables

THIS PAGE INTENTIONALLY LEFT BLANK

Nomenclature

Abbreviations

ANOPP	Aircraft Noise Prediction Program
ARMD	Aerospace Research Mission Directorate
BAF	ANOPP Boeing Airframe Noise Module
BLI	Boundary Layer Ingestion
CFD	Computational Fluid Dynamics
CMI	Cambridge-MIT Institute
CML	Continuous Mold Line
DAMAS	Deconvolution Approach for the Mapping of Acoustic Sources
EPNL	Effective Perceived Noise Level ($EPNdB$)
FAA	Federal Aviation Administration
FAR	Federal Aviation Regulation
FLUENT®	Computational Fluid Dynamics Software Package by Ansys, Inc.
FNKAFM	ANOPP Fink Airframe Noise Module
FPR	Fan Pressure Ratio
FWH	Ffowcs-Williams and Hall
GENSUP	ANOPP General Suppression Module
GRC	Glenn Research Center
HWB	Hybrid Wing-Body
ICAO	International Civil Aviation Organization
ISA	International Standard Atmosphere
LaRC	Langley Research Center

MLW	Maximum Landing Weight
MTOW	Maximum Take-Off Weight
N2A	N+2 project HWB aircraft with conventional podded engines
N2B	N+2 project HWB aircraft with embedded propulsion system
OASPL	Overall Sound Pressure Level (dB)
PNLT	Tone-Corrected Perceived Noise Level (dB)
PSC	Power Savings Coefficient
SAI	Silent Aircraft Initiative
SAX	Silent Aircraft Experimental
SFC	Specific Fuel Consumption
SFWP	Subsonic Fixed Wing Project
SILENCER	Significantly Lower Community Exposure to Aircraft Noise
SPL	Sound Pressure Level (dB)
SST	Shear Stress Transport
TAS	True Airspeed ($knots$)
TRL	Technical Readiness Level
UCI	University of California Irvine
UDF	User Defined Function
UTRC	United Technologies Research Center

Roman Symbols

b_v	Vertical tail span (m)
b_w	Wing span (m)
c	Airfoil chord (m)
c_p	Specific heat at constant pressure (kJ/kg-K)
c_v	Specific heat at constant volume (kJ/kg-K)
C_D	Viscous dissipation coefficient
C_p	Pressure coefficient

$D(\phi, \theta)$	Directivity function
D	Drag (N)
D_t	Doppler factor
$\dot{E}$	Energy outflow (kW)
$\overrightarrow{F}$	Momentum body force term in FLUENT software (N/m^3)
F_n	Net thrust (N)
dh_o	Stagnation specific enthalpy (kJ/kg)
H	Enthalpy (kJ)
I	Far-field noise intensity level (W/m^2)
L	(1) Turbulent wetted edge length or Characteristic Length (m)
	(2) Characteristic Length (m)
M_g	Landing gear local flow Mach number
M_{rel}	Fan face relative Mach number
M_∞	Free stream Mach number
$N1$	Fan speed (rpm)
p	Static pressure (N/m^2)
p^2	Mean square acoustic pressure (Pa^2)
$\langle p_f^2 \rangle^*$	Normalized mean square acoustic pressure
p_{SL}^2	Mean square acoustic pressure at the shear layer (Pa^2)
P_t	Total pressure (Pa)
P	Mechanical power (kW)
P_L,P_M,P_H	Low, medium, and high frequency landing gear noise contributions
P_P	Propulsive power (kW)
P_∞	Free stream total pressure (Pa)
r	Observer distance (m)
R	Gas constant (J/kg-K)
R_a	Apparent noise source to microphone radius (m)
R_m	(1) Meanline fan radius (m)
	(2) Noise source to microphone radius after shear layer refraction (m)
R_o	Free jet centerline to microphone radius along apparent source line (m)

R_s	Shear layer to the microphone radius along apparent source line (m)
R_t	Free jet radius (m)
$R^{'}$	Wave emission radius in still air to the shear layer (m)
s	Specific entropy $(J/K\text{-}kg)$
S	Noise suppression factor
$\dot{S}$	Entropy generation (kW/K)
Sh	Energy body force term in FLUENT software (W/m^3)
St	Strouhal number
T_o	Stagnation temperature (K)
T_{o1}	Stagnation temperature upstream of actuator volume (K)
T_δ	Static temperature at fan blade boundary layer edge (K)
$u^{'}$	Turbulent velocity
u_e	Boundary layer edge velocity (m/s)
u_x	Velocity at axial location (m/s)
$u_{\theta 2}$	Fan stage exit circumferential velocity (m/s)
U	Circumferential fan speed (m/s)
v_t,v_o	Velocity inside and outside of the shear layer (m/s)
V	Noise source volume (m^3)
V_o	Flight velocity (m/s)
V_{ref}	Reference landing speed according to FAR 25.107 $(knots)$
V_2	Reference take-off speed according to FAR 25.107 $(knots)$
V_δ	Fan blade boundary layer edge velocity (m/s)
V_∞	Free stream velocity (m/s)
x,y	Axial and radial coordinate (m)
y^+	Dimensionless wall distance

Greek Symbols

α_f	Atmospheric attenuation

a_∞	Free stream sound speed (m/s)
α_{tip}	Angle of attack relative to the free stream velocity (deg)
β	Fan blade trailing edge metal angle (deg)
γ	Ratio of specific heats
δ_v^*	Vertical tail boundary layer thickness (m)
η_f	Fan efficiency
η_P	Propulsive efficiency
θ	(1) Wave emission angle with Doppler refraction included (deg)
	(2) Fan speed correction parameter
θ_m	Angle from the free jet centerline to R_m (deg)
θ_t, θ_o	Shear layer incidence angle inside and outside of the shear layer (deg)
$\theta^{'}$	Wave emission angle (deg)
θ^*	Kinetic energy thickness (m)
π_f	Fan pressure ratio
Π^*	Acoustic power
ρ_e	Boundary layer edge density (kg/m^3)
ρ_o	(1) Local flow density (kg/m^3)
	(2) Density outside of the shear layer (kg/m^3)
ρ_t	Density inside of the shear layer (kg/m^3)
$\bar{\bar{\tau}}$	Viscous stress tensor (N/m^2)
Φ	Viscous dissipation (kW)
ω	Radian frequency (rad/s)
ω_o	Peak frequency (Hz)
Ω	Fan rotor frequency (Hz)

THIS PAGE INTENTIONALLY LEFT BLANK

Chapter 1

Introduction

Forecasts indicate that world air cargo traffic will increase at 5.8% per year over the next 20 years, tripling current traffic levels, and that the number of cargo aircraft will double [1]. This translates into more than 2,300 new freighter aircraft required for growth and replacement [2]. Aeronautics technology must be advanced to handle such an increase in air traffic from logistical, environmental, and economical viewpoints. That is why NASA's Aerospace Research Mission Directorate (ARMD) sponsors research looking one and two generations ahead of current aircraft, N+1 and N+2, and beyond. Their vision for attainable aircraft requirements to meet the airspace and environmental demands in the 2020 timeframe are outlined in Table 1.1.

Table 1.1: Noise, emission, and fuel burn targets for advanced technologies [3]

	N+1 Generation 2012–2015 Advanced Conventional	N+2 Generation 2018–2020 HWB Aircraft
Noise (cumulative below FAR 36 stage 3)	−42 dB	−52 dB
Emissions (LTO NOx below CAEP/2)	−70%	−80%
Fuel Burn (relative to current equivalent A/C)	−33%	−50%

Hybrid wing-body (HWB) aircraft have emerged as a design well suited to achieve the N+2 goals. They differ from the conventional style flying today in that the entire airframe surface, which is optimized for noise and performance, provides lift. Aircraft design tools as well as noise and performance prediction methodology must also advance as they are mostly based on methods and empirical results from conventional style aircraft. The Massachusetts Institute of Technology (MIT), the University of California Irvine (UCI), Boeing and NASA are working to overcome these challenges together, designing an efficient low-noise HWB aircraft and providing advanced analytical tools for noise and performance evaluation.

The major tasks of the collaborative effort include:

- Define an HWB configuration and identify enabling technologies to meet N+2 fuel burn and noise reduction goals
- Perform initial noise and fuel burn assessments for aircraft
- Propose wind tunnel test methodology to validate noise predictions
- Improve prediction methods for HWB aircraft designs
- Design and build aeroacoustic wind tunnel model with component variability to validate prediction methods
- Validate noise and shielding predictions in wind tunnel test

This thesis details the tools and methodology used to assess the noise levels relative to the N+2 requirements and provides pre-test predictions for the upcoming wind tunnel tests. In addition, a simplified approach is presented to evaluate system performance trends with fan face Mach number for boundary layer ingesting (BLI) propulsion systems. A related thesis [4] provides a detailed description of the N+2 airframe design; therefore, a brief overview is presented first to provide context for the following chapters.

Figure 1-1: SAX-40 Conceptual Aircraft Design [5]

1.1 Silent Aircraft Initiative

The N+2 design builds on a strong foundation of research and design in the area of low-noise efficient aircraft. The Silent Aircraft Initiative (SAI) sponsored by the Cambridge-MIT Institute (CMI) set out to design an aircraft with noise as a primary design constraint and the ultimate goal of reducing aircraft noise below that of a well populated area, or functionally silent [5]. The resulting Silent Aircraft Experimental (SAX-40) HWB is the basis for the N+2 design. The SAX-40 has an estimated 63 dB effective perceived noise level (EPNL) on takeoff and approach (more than 35 dB below Stage 3) and an estimated fuel burn of 124 passenger miles per gallon (25% below current comparable aircraft).

The SAX-40 achieves this significant noise reduction while also improving aircraft performance by using an HWB design and an embedded distributed propulsion system as illustrated in Figure 1-1 [5]. Where airframe noise is a function of flight speed, the all-lifting body is designed for enhanced low-speed performance on take-off and approach. Trim and stability control provided by aerodynamic shaping of the centerbody leading edge at cruise and thrust vectoring during take-off and landing enables this tailless design and eliminates additional control surfaces that would otherwise contribute to the overall noise level. The distributed propulsion system uses three embedded engine clusters in the wing suction surface. Each cluster has one high-pressure engine core and low-pressure turbine that drives three fans, as shown in Figure 1-2. The resulting high bypass ratio and airframe BLI provide a propulsive

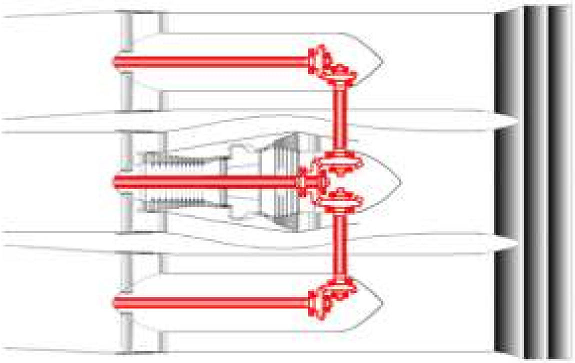

Figure 1-2: Schematic layout of SAX-40 tri-cluster engine system [6]

efficiency benefit and the low jet velocity and fan speed reduce engine noise. Embedding the engines also provides shielding of the fan forward noise. Finally, noise reduction features such as continuous mold lines between flaps and ailerons, trailing edge brushes, deployable drooped leading edges and acoustic duct liners all enable this step change in overall noise level.

1.2 N+2 Preliminary Airframe Design

A cargo freighter aircraft is chosen as the entry application for the N+2 HWB with design requirements of 6000 nm range and 103,000 lb payload capability, an increase of 20% and 100% over the passenger SAX-40, respectively. The technology readiness level (TRL) requirement is 5 to 6 by 2012 with entry into service (EIS) by 2020 [3]. This TRL requires a technology demonstration in a relevant environment that will be satisfied with a wind tunnel test.

The preliminary cargo aircraft design dubbed the SAX-40F leverages the existing SAX-40 centerbody design and MIT's quasi 3-D airframe design methodology developed for SAI [4]. Lift and moment distributions along with induced drag are calculated using the vortex lattice method, AVL[7], and outer wing viscous and shock wave drag are estimated with the viscous 2-D airfoil design tool, MSES[8]. The flow around the centerbody cannot be modeled using 2-D tools due to 3-D flow relief; therefore, empirical relationships for bodies of revolution are used for drag calculations. This combination of tools yields the fidelity required for initial design optimization

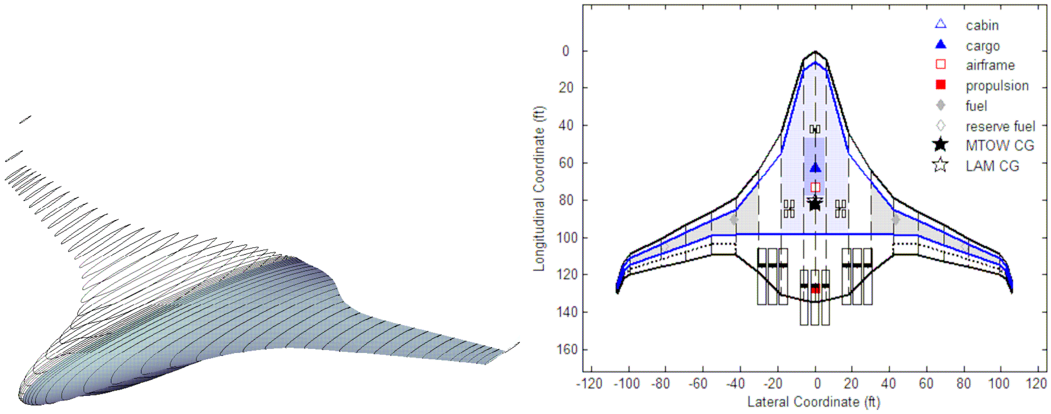

Figure 1-3: SAX-40F Design [4]

of the centerbody [9].

Several design modifications were required to convert the SAX-40 passenger aircraft to a freighter version meeting the range and cargo requirements. The key changes are listed below and the design illustrated in Figure 1-3.

Structural Modifications

- Wing span reduced to 211.6 ft. meeting International Civil Aviation Organization (ICAO) Code E category requirements (B747-400)
- Rear spar moved aft by 33" to accommodate containers
- Interior layout for the main and lower deck adjusted for the cargo payload
- Fuel distributed along the outer wings, starting at the wing tips
- Outer wing twist and sweep increased and moved aft to maintain static stability

Weight Adjustments

- Engine weight scaled up by 32% based on greater top of climb thrust
- Fixed equipment weight reduced to freighter configuration
- Structural weight updated based on greater gross weight

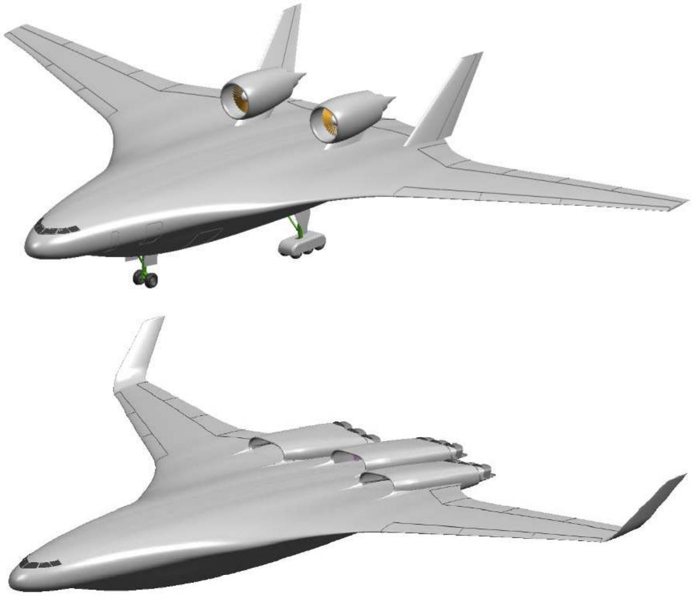

Figure 1-4: Boeing N2A (upper) and N2B (lower) configurations based on the SAX-40F design [picture courtesy of D. Odle, Boeing]

1.3 N2A and N2B Designs

Boeing expanded on the MIT SAX-40F planform design, integrating the propulsion system in two different configurations shown in Figure 1-4. The N2A utilizes two podded engines that are positioned outside of the airframe boundary layer. The winglets are removed and replaced with two vertical stabilizers situated closer to the engine exhaust for enhanced sideline noise shielding. The engines are also positioned slightly forward for additional fan rearward and jet noise reduction. The wingspan is increased to account for the removal of the winglets. The N2B retains the SAX-40F planform, embedding the propulsion system in the suction surface trailing edge. The N2A design will be used to design and advance performance and noise modeling techniques with validation in wind tunnel tests. The N2B design concept is of higher risk and separate research efforts are underway focused on embedding the propulsion system and exploring distortion tolerant fan designs.

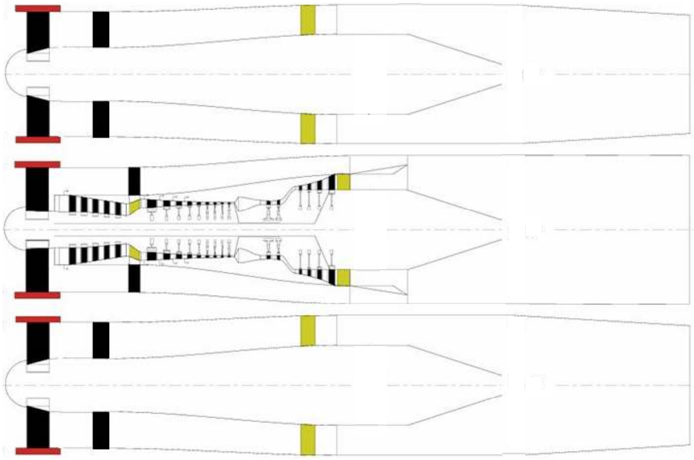

Figure 1-5: Schematic layout of the GRC tri-cluster engine system [10]

1.4 N2A and N2B Propulsion Systems

NASA Glenn Research Center (GRC) conducted the propulsion system conceptual design and modeling [10]. The N2A utilizes 1.6 fan pressure ratio (FPR) direct-drive engines producing approximately 68,000 lbf static thrust at sea level and 15,000 lbf at top-of-climb. The two-spool system consists of a fan with booster stages, axial compressor, cooled high-pressure turbine and uncooled low-pressure turbine. The N2B incorporates three engine sets similar to the Granta engine [6] with a direct-drive 1.5 pressure ratio fan and two geared fans, shown in Figure 1-5. Each engine cluster produce approximately 49,000 lbf static thrust at sea level and 8,300 lbf at top-of-climb. The high-pressure compressor is purely axial; however, it is possible to use an axial-centrifugal configuration similar to the Granta engine to increase overall pressure ratio and decrease the axial length of the core. Minimizing the core length reduces the length and weight of the fan drive system and allows for longer exhaust duct acoustic liners.

1.5 Noise Assessment

Chapters 2 and 3 examine the noise characteristics of the N2A and N2B aircraft and propulsion systems described above. Previous research recognized that current noise prediction tools are insufficient to predict HWB aircraft noise and therefore augmented pre-existing empirical tools with first principle methodologies adapted to HWB designs [11]. The analysis in this thesis leverages this approach, using relevant airframe and engine noise modules from NASA's Aircraft Noise Prediction Program (ANOPP) while investigating limitations of applying ANOPP to HWB aircraft and identifying areas for improvement. An improved airfoil self–noise model is implemented that follows SAI methodology using boundary layer properties rather than empirical relationships based on airframe geometry. In addition, shielding estimates are improved based on UCI and SAX-40 research. ANOPP is used to bring the noise contributions together for a preliminary Federal Aviation Regulation (FAR) Part 36 certification estimate. Finally, the full-scale noise estimates are then used to generate pre-test predictions for the N2A model-scale wind tunnel test.

1.6 N2B Propulsion System Integration

Chapter 4 progresses beyond the noise advantage of the HWB aircraft and investigates the N2B propulsion system integration. Inlet total pressure distortion and pressure recovery are two design risks involved with the embedded propulsion systems. The internal flow of the engine and the external flow of the aircraft are coupled by the fan inlet conditions and the ingested boundary layer creates a non-uniform total pressure distribution at the fan face. This requires a distortion tolerant fan design [12]. Chapter 4 describes how an increased fan face Mach number can potentially decrease the boundary layer thickness for total pressure distortion risk mitigation. The study also suggests that BLI can provide a propulsive efficiency benefit that reduces the mechanical power required for steady level flight. A 2-D computational domain with contoured slip boundaries around the centerbody is used to replicate the effects of 3-D relief on the airframe and inlet aerodynamics. The domain includes the S-shaped inlet duct and is extended far downstream for a Trefftz plane power balance analysis to determine the propulsive power required for steady level flight. This allows the airframe, inlet, and fan efficiency interactions to be simulated as a function of fan face Mach number and evaluate performance trends.

1.7 Contributions

The contributions of this thesis are:

1. Establishment of ANOPP based noise assessment methodology for HWB airframe configurations and preliminary N2A and N2B FAR Part 36 certification estimates that define the required technological improvements to meet the NASA N+2 goals.
2. Wind tunnel model scale noise predictions for pre-test planning and definition of test limitations.
3. Development of a simplified propulsion system integration study using a power balance analysis capable of exploring guidelines for fan system designs with BLI.
4. Quantification of BLI power savings trends as a function of fan face Mach number and recommendations for future detailed N2B inlet design.

THIS PAGE INTENTIONALLY LEFT BLANK

Chapter 2

N+2 Noise Assessment

The NASA Aircraft Noise Prediction Program is used for the N+2 assessment. Noise prediction methodology and empirical databases, such as those found in ANOPP, are largely based on conventional commercial aircraft. Conventional in this context refers to airframes composed of a cylindrical fuselage, relatively high aspect ratio wings, and a tail with horizontal and vertical stabilizers. In addition, the engines are generally mounted either below the wing or aft on the fuselage. Therefore, ANOPP is used in this analysis while investigating which noise modules are applicable to HWB aircraft and those that need to be modified or replaced for the N+2 analyses. The N2A and N2B aircraft noise levels are then assessed relative to the goals outlined in Table 1.1, which apply to the FAR Part 36 noise certification procedure.

2.1 FAR Part 36 Assessment Procedure

The FAR Part 36 noise certification analysis is conducted at International Standard Atmosphere (ISA) reference conditions plus 10 °C, 70% relative humidity, zero wind, and sea level. Noise certification measurement locations are required at the approach, lateral and flyover observer locations that are shown in Figure 2-1.

Special flight trajectories that provide additional noise reduction were not considered in this analysis since the intent is to compare the overall noise level to other commercial aircraft, subject to the current FAR ground rules summarized below. The

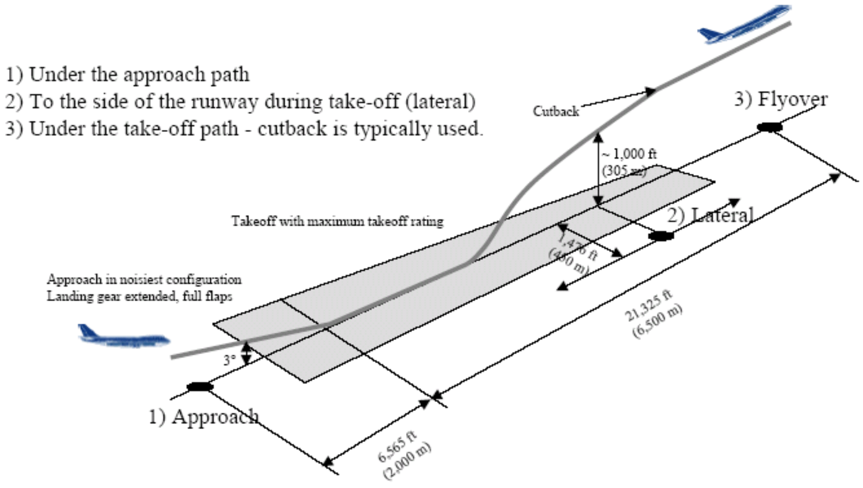

Figure 2-1: FAR Part 36 noise measurement locations (courtesy of A. Mortlock - Boeing)

overall noise level is measured as EPNL in decibels (EPNdB) as specified by the Federal Aviation Administration (FAA). This captures not only the sound pressure level, but also the tonal and duration effects on the human perception of noisiness. The procedure for calculating this value is governed by Section FAR Part A36.4.

<u>Flyover</u>

- Maximum Take-Off Weight (MTOW)
- Monitor point at 21,325 ft from brakes release
- Maximum takeoff power from brakes release
- $V_2 + 10$ knots climb-out speed
- Thrust cutback performed at 3,000–4,000 ft before monitor
- Instantaneous cutback flight profile assumed

Lateral

- MTOW
- Maximum takeoff power
- $V_2 + 10$ knots climb-out speed
- Noise monitor at 1,476 ft to the side of the runway extended centerline
- Initial peak lateral observer noise assumed to occur at 1,000 ft above ground level, representing an angle of elevation from monitor to aircraft of $34.1\,^\circ$
- No impact of cutback procedure on peak lateral observer noise allowed

Approach

- Maximum landing weight (MLW)
- Approach monitor at 6,565 ft from runway threshold (394 feet)
- Aircraft to maintain $-3\,^\circ$ glide-slope
- Noisiest configuration (usually dirtiest aerodynamic - highest drag condition)
- $V_{ref} + 10$ knots TAS approach speed

The aircraft and engine parameters used for lateral, flyover, and approach observer noise estimates at the reference conditions are summarized in Table 2.1 for the N+2 aircraft.

2.2 Noise Sources and Estimation Methods

The noise sources summarized in Table 2.2 and the low noise enabling technologies in Figure 2-2 are considered in the overall noise estimation. A detailed description of the noise estimation methods and key technologies are provided in Section 2.3. NASA GRC provided the propulsion system noise estimates and the methods used are listed in Table 2.2 in italics as a reference to the respective ANOPP modules.

Table 2.1: N2A and N2B aircraft and engine performance data

	N2A			N2B		
Parameter	Lateral	Flyover	Approach	Lateral	Flyover	Approach
Flight Angle (°)	9.5	2.3	-3.0	9.0	2.3	-3.0
Angle of Attack (°)	13.4	13.9	10.7	13.4	14.0	10.7
Elevon Angle (°)	-10	-10	-10	-20	-20	-20
F_n/δ/engine (lbs)	68,056	28,612	4,434	38,711	19,781	2,937
$N1/\sqrt{\theta}$ (rpm)	3,018	2,320	1,335	5,470	4,341	2,540
Altitude (feet)	1,000	2,104	394	1,000	2,178	394
TAS (kts)	145	147	146	148	151	147

Table 2.2: Summary of noise source and shielding estimation methods

Noise Source	Estimation Method
Fan, forward propagating	ANOPP Heidmann Fan Module, *GE Large Turbofan Method* TREAT acoustic liner increments, *GE Large Turbofan Method* SAX-40 ray-tracing shielding increments
Fan, rearward propagating	ANOPP Heidmann Fan Module, *GE Large Turbofan Method* TREAT acoustic liner increments, *GE Large Turbofan Method* Beranek & Maekawa barrier shielding increments (N2A only)
Core	ANOPP GE Core Module Beranek & Maekawa barrier shielding increments (N2A only)
Jet (N2A)	ANOPP Stone 2 Jet Module UCI jet noise shielding increments with perforated wedge
Jet (N2B)	Scaled Granta (SAX-40) jet hemisphere
Undercarriage	Modified ANOPP Boeing Airframe Module Faired landing gear noise reduction increments
Elevon	ANOPP Boeing Airframe Module (modeled as aileron) Trailing Edge Continuous Mold Line
Leading Edge Droop	Droop effect on BL properties included in FW-Hall method Leading Edge Continuous Mold Line
Wing	Physics-based airfoil self-noise method (FWH)
Wing Tip (N2A) Winglet (N2B)	Tip vortex noise model from Brooks and Marcolini
Vertical Tail (N2A)	ANOPP Fink Airframe Module

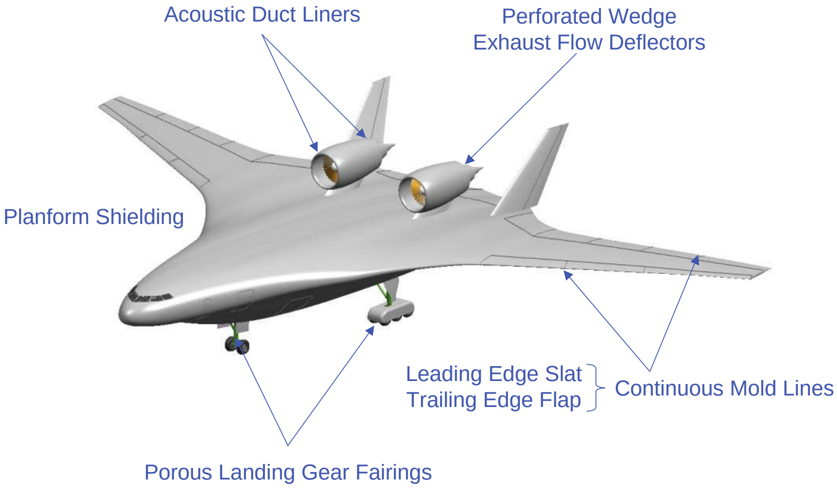

Figure 2-2: Low-noise enabling technologies for the N2A (isometric view courtesy of D. Odle - Boeing)

2.2.1 Airfoil Noise

Airfoil self-noise due to the scattering of turbulent flow structures of the airframe boundary layer near the wing trailing edges is estimated using a technique originally introduced by Manneville et al. [13] and further developed by Hileman and Spakovszky [14] for the SAX aircraft. This method builds on the work by Ffowcs-Williams and Hall (FWH) that models the noise amplitude of turbulence generated noise at the trailing edge of a semi-infinite flat plate using the Lighthill acoustic analogy [15]. The FWH equation as presented by Lockard and Lilley [16] and derived by Goldstein [17] gives the far-field noise intensity level per unit volume,

$$\frac{I}{V} = \frac{a_\infty^3 \omega_o \rho_o^2 u'^4}{\rho_\infty 2\pi^3 r^2 a_\infty^5} \tag{2.1}$$

where a_∞ is the free stream sound speed, ρ_o is the local flow density, and r is the observer distance. The peak frequency, ω_o, volume enclosing the turbulent eddies, V, and turbulent velocity, u', are related to boundary layer quantities that are calculated using a 2-D viscous airfoil analysis software package, XFOIL.

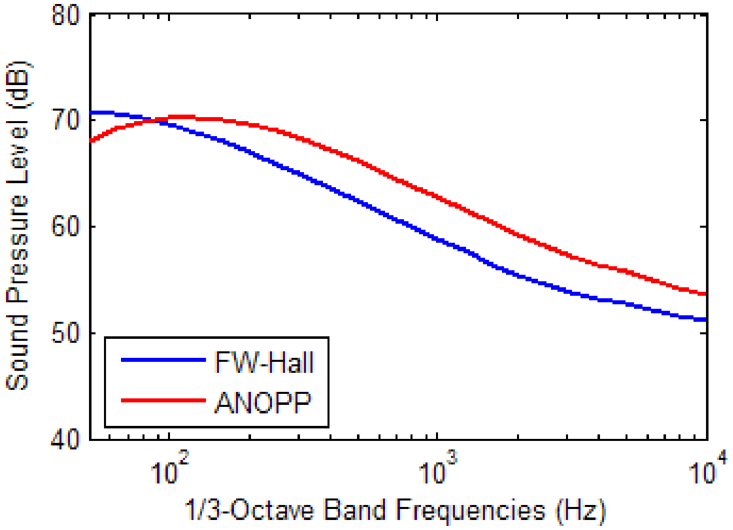

Figure 2-3: Comparison of airfoil noise spectra between FWH method and ANOPP's airframe noise method by Fink [figure courtesy of L. Ng]

Empirical relations are used for the peak frequency and spectral shapes. The former is based on data by Lockard and Lilley [16] and includes a Doppler frequency shift correction. The latter uses the Fink model [18] for conventional wings, as opposed to delta wings, based on the aerodynamic analysis of the SAX-40. The centerbody did not exhibit leading edge vortex shedding as it can occur on delta wing type planforms which leads to increased high frequency noise levels [19].

The FWH method and ANOPP's airframe noise method by Fink are applied to the N2A aircraft to produce the airfoil noise spectra in Figure 2-3. The plot shows similar amplitudes between the two methods with the FWH method producing a lower peak frequency. The suction surface has an order of magnitude larger displacement thickness that dominates the overall noise and leads to the lower peak frequency. The overall sound pressure level calculated with the FWH method, 78.9 dB, is within 2% of that calculated by ANOPP, 80.1 dB. This confirms the finding by Hileman [14] that the FWH method is capable of predicting airfoil self-noise with the same fidelity as ANOPP but has the advantage of using a physics-based model that links boundary layer properties to the noise amplitude.

2.2.2 Wing Tip (N2A) and Winglet (N2B) Noise

The N2A wing tip and N2B winglet noise levels are estimated using the empirical method introduced by Brooks and Marcolini [20][21]. The noise generation mechanism is the interaction of the wing tip vortex and the turbulent flow at the wing trailing edge. Highly turbulent flow is introduced over the trailing edge and generates more turbulence scattering noise than would occur without the tip vortex. Brooks and Marcolini isolated the tip vortex formation noise from wind tunnel test data and developed a semi-empirical noise prediction model based on trailing edge noise theory and aerodynamic analysis. The sound pressure level is given by,

$$SPL = 10\log\left(\frac{2M_{\infty}^{5}(1+0.036\alpha_{tip})^{3}L_{tip}D(\phi,\theta)}{r^{2}}\right) - 30.5(\log(St)+0.3)^{2} + 126 \qquad (2.2)$$

where M_{∞} is the free stream Mach number, α_{tip} is the angle of attack relative to the free stream velocity, L_{tip} is the turbulent wetted length of the edge, D is the directivity function, and St is the Strouhal number. Whereas this additional wing tip vortex contribution is included in the empirical wing trailing edge noise model in ANOPP, it is important to add this noise to the FWH method assessment.

2.2.3 Landing Gear Noise

The undercarriage noise is estimated using ANOPP's Boeing Airframe Noise Module (BAF) [22]. The BAF formulation, developed by Guo [23][24], is based on semi-empirical correlations established from full-scale test data. The normalized mean square acoustic pressure is expressed as,

$$\langle p_f^2\rangle^* \propto M_g^6(P_L + P_M + P_H) \qquad (2.3)$$

where M_g is the flow Mach number local to the landing gear and P_L, P_M, P_H are low, medium, and high frequency component contributions to the overall noise, respectively. The tires (low frequency), shock struts (mid frequency), and small features or irregular geometries (high frequency) each have separate correlations for radiation efficiency, amplitude, directivity, and frequency spectrum functions. The peak acoustic pressure is primarily a function of the landing gear surface area and the complexity, characterized by the number of components and weight of the aircraft.

Most conventional aircraft experience a local flow velocity suppression in the vicinity of the main landing gear that is caused by the lifting force on the wing, which is why the BAF formulation uses M_g. The surface vorticity distribution in the lifting flow field induces an increased velocity above the wing and a decreased velocity below the wing relative to free stream. In fact, a study of commercial landing gear found that wing lifting effects reduced free stream velocity by 20 to 30% [25]. The ANOPP model by Guo uses a 0.75 suppression factor on free stream Mach number to estimate the local value.

Preliminary CFD for the N2A planform indicates the main landing gear experience no local suppression. This is relevant as the acoustic power scales with Mach to the sixth power[1]. In addition, the Strouhal number used in the narrow band spectral function is both a function of local and free stream Mach numbers. Therefore, the constant scale factor was removed and made variable such that the local Mach number can be specified for any airframe. Boeing 777 model scale wind tunnel data, where Mach suppression is not present, compared well with ANOPP predictions using a suppression factor of one, validating this method.

The main landing gear set is assumed to employ a porous fairing to counteract the lack of Mach suppression and reduce noise. A porous fairing is used to reduce flow velocity over the fairing and reduce recirculation. Model scale wind tunnel tests completed as part of the SILENCER program (Significantly Lower Community Exposure to Aircraft Noise) evaluated this configuration and a wide fairing that extends to cover the brakes that achieved a 3 to 6 dB reduction over the baseline configuration across the frequency spectrum [26].

The landing gear module in ANOPP does not account for noise reduction devices. For this analysis, the estimated noise reduction was applied to the baseline main

---

[1] Landing gear in low Mach number flow can be modeled as bluff bodies where vortices shed in alternating patterns resemble a dipole source

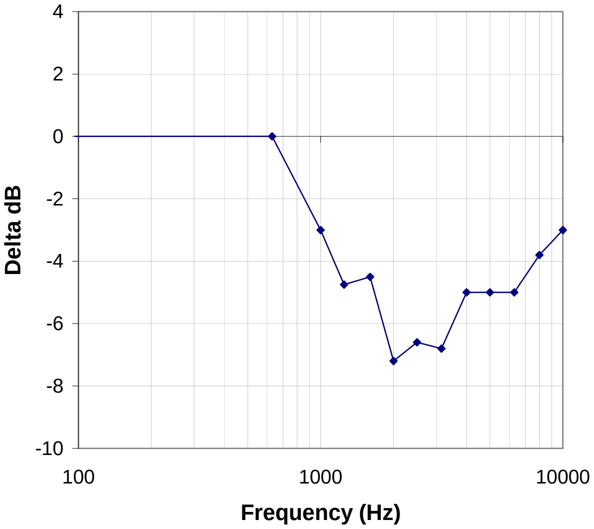

Figure 2-4: Noise reduction levels due to fairing on main landing gear (adapted from Smith et al. [26])

landing gear noise using the ANOPP General Suppression Module (GENSUP) [27]. The noise reduction, in terms of ΔdB, are converted to a suppression factor,

$$S = \frac{\langle p^2 \rangle_s^*}{\langle p^2 \rangle^*} \tag{2.4}$$

which is the ratio of suppressed to unsuppressed normalized mean squared acoustic pressure. Nominally, the suppression factor is supplied for directivity and azimuthal angles defining a hemisphere below the aircraft at all frequency levels. The hemisphere is then interpolated by ANOPP for each directivity and azimuthal angles prior to propagation of the noise from the aircraft to the observer. In this case, the noise reduction levels for the fairing in Figure 2-4 were assumed to be a function of only frequency.

2.2.4 Elevon Noise

The elevon side edge noise was estimated with the aileron component of the ANOPP BAF Module. This module is chosen over the flap model because the elevons do not have slots like conventional flaps and most resemble ailerons. This formulation developed by Sen et al. [28][29], is based on Boeing's database of model-scale wind

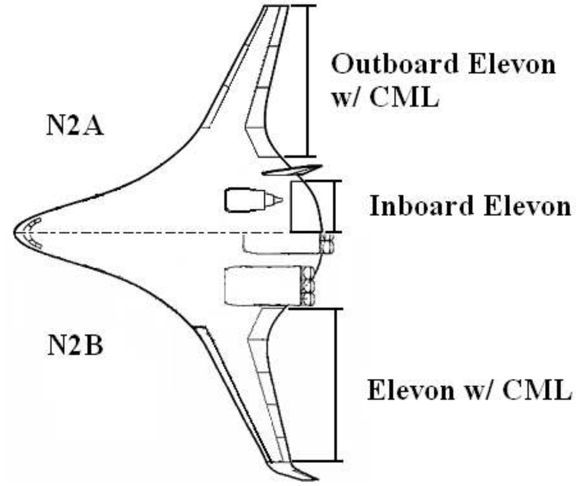

Figure 2-5: Control surface geometry for the N2A (upper) and N2B (lower)

tunnel data.

The trailing vortices resulting from a lift discontinuity between elevon side edges generate turbulent flow and noise. This is the same noise generation mechanism that is present between a conventional flap and aileron. The higher lift coefficient of the outboard flap drives the magnitude of the lift discontinuity; therefore, the BAF module correlates the overall sound pressure to the lift coefficient, chord, and deflection angle of the outboard flap, not the aileron.

The elevon section average lift coefficient and chord is used for the N2A and N2B noise prediction. The parameters for each elevon or grouped elevons were used in place of the outboard flap parameters generally used in the assessment of conventional aircraft configurations. The elevons are illustrated in Figure 2-5. For the N2A airframe, the control surfaces were treated as two individual elevons, one each inboard and outboard of the vertical tail surfaces for a total of four side edges. The outboard elevon, which has four independent control surfaces, is assumed to use continuous mold-line (CML) trailing edge technology that eliminates the interior side edges. Similarly, the N2B has five elevons using a CML trailing edge leaving only two side edges.

The span load was calculated during the airframe design using AVL as described in Chapter 1. The N2A span load data shown below in Figure 2-6 compares well

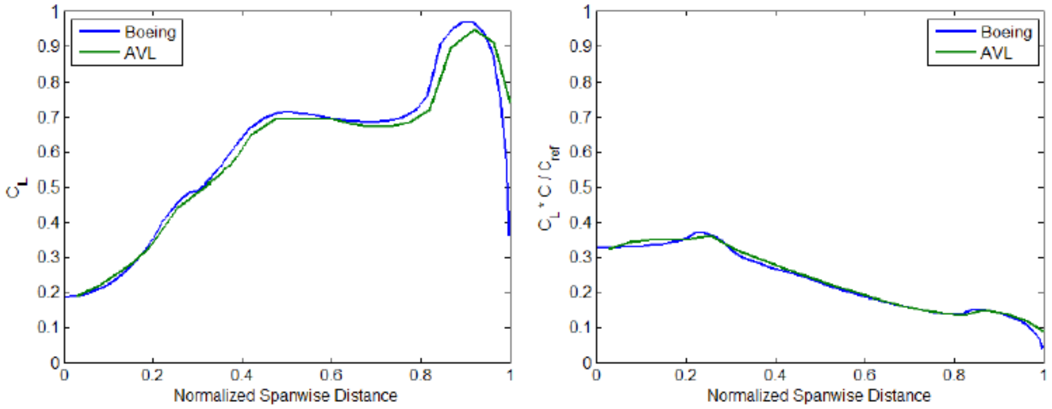

Figure 2-6: N2A approach span load compared with Boeing three-dimensional Navier-Stokes calculation [4]

with the 3-D CFD span load calculations by Boeing for the approach configuration, validating the method. Therefore, AVL was used to calculate the lift coefficients of the elevons as inputs to the noise module.

2.2.5 Leading Edge Droop

The leading edge high-lift device was modeled as a drooped leading edge. A slat is often extended on the leading edge to reduce stalling speed and increase lift. This creates a gap in the wing leading edge and noise is generated in the slat cove. A drooped leading edge eliminates this gap and reduces noise. However, there is a contribution to noise as the drooped leading edge changes the boundary layer and the properties of the turbulent flow structures scattered at the airfoil trailing edge. This effect is included as part of the XFOIL calculations in the FWH airfoil noise method described in Section 2.2.1. A side edge noise model is not required as a CML leading edge is used.

2.2.6 Vertical Tail Noise (N2A Only)

The N2A vertical tail noise is estimated using the Airframe Noise Module (FNKAFM) available in ANOPP [30]. This method, developed by Fink [18], is based on flyover monitor data from a variety of airframes such as large commercial aircraft, business jets, delta wings, and high-performance sailplanes. The acoustic power is expressed as,

$$\Pi^* \propto M_\infty^5 \cdot \delta_v^* \left(\frac{b_v}{b_w}\right) \tag{2.5}$$

where δ_v^* is the vertical tail boundary layer thickness, b_v is the vertical tail span, and b_w is the wing span. The boundary layer properties are based on a flat plate analysis, which requires area and span geometric inputs. The vertical tail has simple control surfaces and can be assumed aerodynamically clean, reducing the acoustic power level.

2.3 Noise Shielding Increments

The engines are podded above the wing planform in the N2A and are embedded in the aft suction surface of the N2B centerbody, which provides a noise shielding benefit. A combination of previous noise shielding results, existing methods, and empirical data are used in this preliminary analysis. Table 2.3 provides a summary of the noise shielding increments (ΔdB) at the peak directivity angles. Substantial shielding is present in the forward direction in both the N2A and N2B and in the rearward direction for the N2A. As will be discussed in Section 2.4, additional jet noise shielding and noise reduction techniques are required to reach the N+2 goals.

Table 2.3: Noise shielding increments applied at peak directivity angles

	N2A ΔdB at Peak			N2B ΔdB at Peak		
	Flyover	Lateral	Approach	Flyover	Lateral	Approach
Fan Fwd	24.4	22.6	23.5	27.1	23.5	25.0
Fan Rwd	19.6	14.9	19.6	–	–	–
Core	19.4	12.0	19.2	–	–	–
Jet	3.8	3.6	5.1	–	–	–

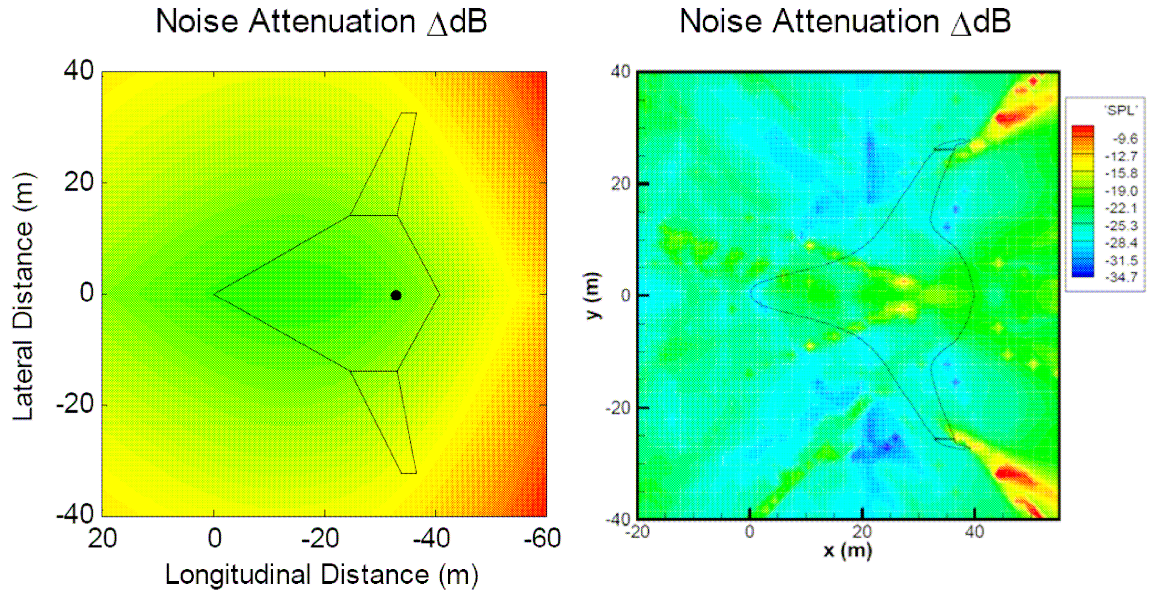

Figure 2-7: Shielding comparison of a monopole using (a) Beranek and Maekawa barrier shielding [4] and (b) ray-tracing hemispheres [31]

2.3.1 Fan Forward Shielding

Ray-tracing data from the SAX-40 is used to estimate fan forward shielding in this analysis. Ray tracing predicts the path of acoustic waves accounting not only for wave diffraction at sharp edges but also creeping rays that follow the rounded airframe edges [31]. The N+2 planforms are very similar to the SAX-40 and due to tool availability and time constraints the SAX-40 shielding hemisphere is applied directly to the preliminary N2A and N2B assessments.

The ray-tracing based results are compared with the ANOPP barrier shielding method [32] in Figure 2-7. The barrier shielding method, based on the work of Beranek and Maekawa [33][34], is unable to capture the shielding effects of complex geometries as it based on the shielding of semi-infinite rectangular barriers. The method does not capture the impact of the winglets where rays are diffracted around the winglet reducing the noise shielding. An improved method is implemented by Ng [4] that determines the complete shielding edge of any 3-D object and applies the diffraction integral along the entire contour. The advantage of the diffraction integral method is that it provides a level of fidelity much closer to ray-tracing than barrier shielding but with the reduced computational complexity required for ANOPP. However, the diffraction integral method does not capture creeping rays and is better suited for thin objects with relatively sharp edges. This method was not available for this analysis and more information can be found in Ng [4].

There are differences between the SAX-40 configuration and the N+2 aircraft that could alter the results when a more detailed shielding assessment is completed. The shielding hemisphere is based on three podded fans and an airframe with winglets. The N2A propulsion system consists of two podded engines and vertical tails replace the winglets. The differences in the shielding will be assessed using the updated diffraction integral method in future noise audits. The shielding hemisphere used for the N2B aircraft with an embedded, distributed propulsion system is consistent with the configuration used in the ray tracing calculations.

2.3.2 Fan Rearward and Core Shielding (N2A Only)

N2A fan rearward and core noise suppression was estimated using the ANOPP barrier shielding method. The wing planform was approximated with four points forming the leading and trailing edges from root to tip. As previously mentioned, the Wing Module cannot estimate the noise suppression from the N2A vertical tail. Future assessments will use the diffraction integral method described in 2.3.1.

2.3.3 Jet Shielding (N2A Only)

Jet shielding was estimated based on scale-model wind tunnel tests conducted by UCI [35]. Noise from a cold jet was shielded with a flat plate representation of a 1.1% scale-model N2A planform including the vertical fins. Shielding derivatives were obtained for engine positions forward and aft of the nominal location, alternate vertical tail dihedral angles, and with a perforated wedge jet flow deflector. A deployable wedge is located at the 12 o'clock position of the jet flow which deflects the exhaust stream downward and increases the shielding by 2-3 dB. Data from the nominal engine position with a perforated-flap jet flow deflector was used in this analysis.

Test data was only available for directivity angles of $50 - 70\,^{\circ}$ in $5\,^{\circ}$ increments and azimuth angles $0 - 90\,^{\circ}$ in $30\,^{\circ}$ increments due to the experimental setup in the anechoic chamber. This limits the ability to estimate shielding in the forward direction. Shielding would tend to increase as the directivity angle decreases below $50\,^{\circ}$; therefore, the overall jet noise is slightly pessimistic.

2.4 FAR Part 36 Noise Certification Results

The noise sources and installation effects in Table 2.2 were combined using ANOPP to assess the overall aircraft noise at the FAR Part 36 observer locations. Table 2.4 summarizes the N+2 aircraft assessments for lateral, flyover, and approach observer locations. Time history traces are presented below that illustrate the breakdown of each noise source along the flight trajectory. The results indicate that engine noise must be reduced to achieve the N+2 noise goals with elevon side edge and main landing gear noise being the next largest noise contributors.

Table 2.4: Summary of N2A and N2B Noise Assessment

Noise Certification Conditions	N2A (EPNdB)	N2B (EPNdB)
Lateral	90.1	94.1
Flyover	76.9	87.0
Approach	86.8	93.6
Cumulative	253.8	274.7
Delta from N+2 Goal	-5.3	-26.2

2.4.1 N2A Tone-Corrected Perceived Noise Levels

The N2A aircraft noise estimate shows promise of meeting the N+2 goal, with an additional 5.3 dB reduction required to achieve 52 dB below stage 3 limits. The lateral observer location noise levels shown in Figure 2-8 are primarily set by engine noise, in particular the rearward propagating components. The jet and fan rearward sources are 20 dB above the next loudest sources, the core and fan forward noise. Therefore, one way to reduce the noise at the lateral observer location is to decrease

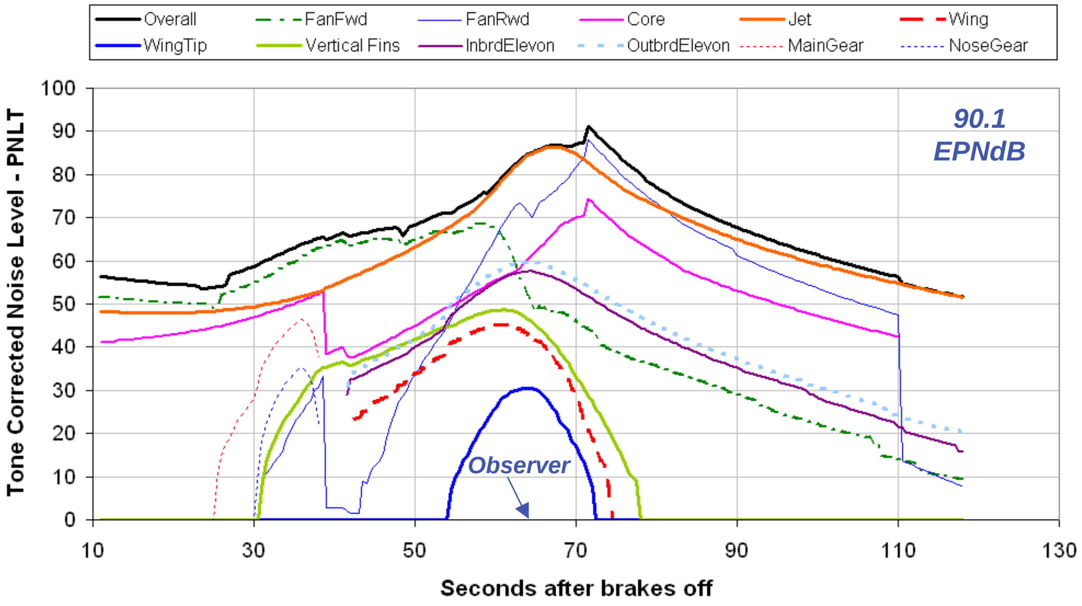

Figure 2-8: N2A lateral PNLT and EPNL estimates

the fan exit velocity with a lower fan pressure ratio. The peak in fan rearward noise around 71 seconds, when the observer is no longer in the shielding shadow region, also emphasizes the need to assess the noise with the diffraction integral method. This would then utilize the entire shielding outline, including the vertical tail, which could decrease observed noise. Outside of analytical improvements, changes to the airframe geometry such as increasing the length of the inboard elevons would provide additional shielding and noise reduction.

The jet and fan rearward noise sources are again the loudest components at the flyover observer location (Figure 2-9); however, the thrust cutback at 91 seconds provides a 15 to 20 dB noise reduction above the observer relative to the lateral noise location. This reduces the engine noise to levels comparable with the airframe noise where ailerons will limit any engine noise shielding improvements. Extending the continuous mold line across the remaining side edges or decreasing the deflection angle through thrust vectoring are two possible methods to eliminate or reduce the side edge noise. This is also the case for approach noise (Figure 2-10) where the elevons will inhibit noise reduction from landing gear improvements.

Whereas the main landing gear are retracted early on the take off trajectories,

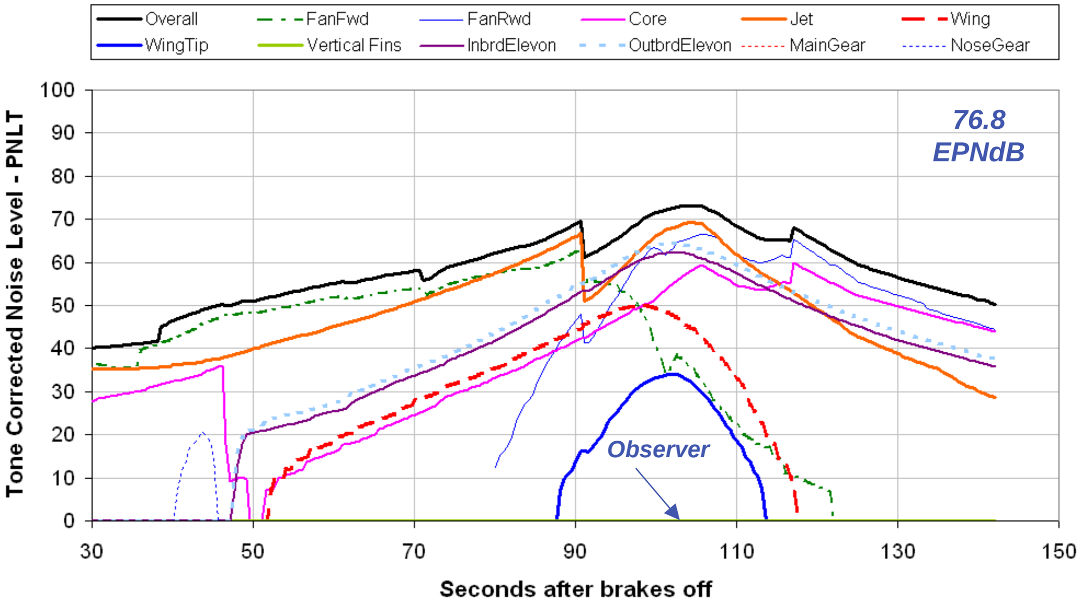

Figure 2-9: N2A flyover PNLT and EPNL estimates

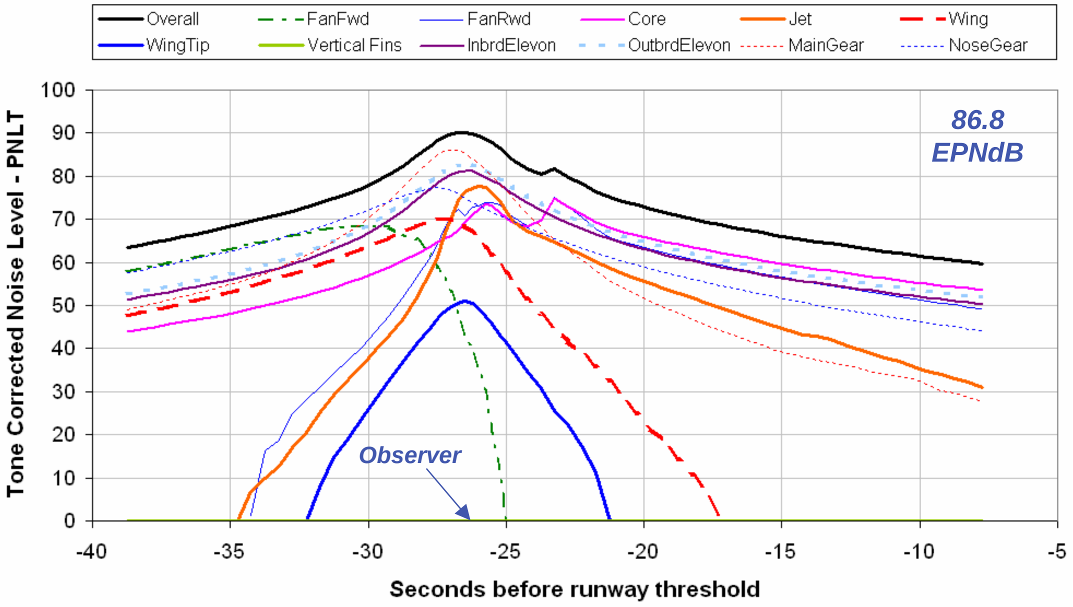

Figure 2-10: N2A approach PNLT and EPNL estimates

they are deployed on approach and are the most dominant noise source. The N2A configuration does not benefit from the local velocity suppression that most conventional aircraft experience as discussed in Section 2.2.3. Fairings are utilized in this configuration, reducing the main landing gear contribution by about 2.2 dB; however, the benefit to the overall noise is less than 1 dB due to the jet and elevon noise levels. More advanced landing gear designs in addition to fairings may be required to further reduce landing gear noise. Dobrzynski et al. [36] investigated advanced designs that reduced the number of braces required to support the main landing gear while improving the aerodynamics of the large main strut. Noise reductions on the main and nose landing gear assemblies were on the order of 4 to 6 dB, respectively, and 10 dB noise reductions are targeted for 2020 time frame.

2.4.2 N2B Tone-Corrected Perceived Noise Levels

The preliminary N2B aircraft noise estimate requires an additional 26.2 dB reduction to meet the N+2 goals. However, it is important to note that the ANOPP noise modules are not well suited for the tri-cluster engines of the N2B and the overall levels are likely overestimated. As such, more work is necessary to bring the fidelity of the noise assessment to the same level as that of the N2A aircraft. For example, ANOPP does not appropriately model the mixing of the fan and core exhaust streams and under predicts the liner noise attenuation. A scaled Granta SAI jet noise estimate is used for this report as a rectangular nozzle configuration is currently not available. The N2B engine noise estimates should improve as more advanced models are incorporated into ANOPP and begin to close the gap between the initial assessment and the SAX-40. The estimated noise levels for the SAX-40 were 69.2 dB, 68.8 dB, and 71.4 dB for lateral, flyover, and approach observers using a similar configuration [11] beating the N+2 goals by 39.1 dB.

The N2B elevon noise is reduced relative to the N2A by approximately 2 dB by eliminating the side edge between the inboard and outboard elevons. This allows for additional noise reduction if the engine noise can be lowered to the airframe levels. Engine noise estimates will likely not be reduced with diffraction integral method shielding analysis, as the fan rearward and jet noise sources are unshielded. Finally, increased duct liner length may be increased for additional noise reduction. Increasing the length from the current baseline, 150 inches, to the full duct length, 263 inches, provides and additional 2.6 dB decrease in overall perceived noise levels. However, this incurs a weight penalty that will affect overall aircraft performance. Therefore, higher fidelity methods to optimize liner noise attenuation such as those implemented by Law and Dowling [37] for SAI may be required.

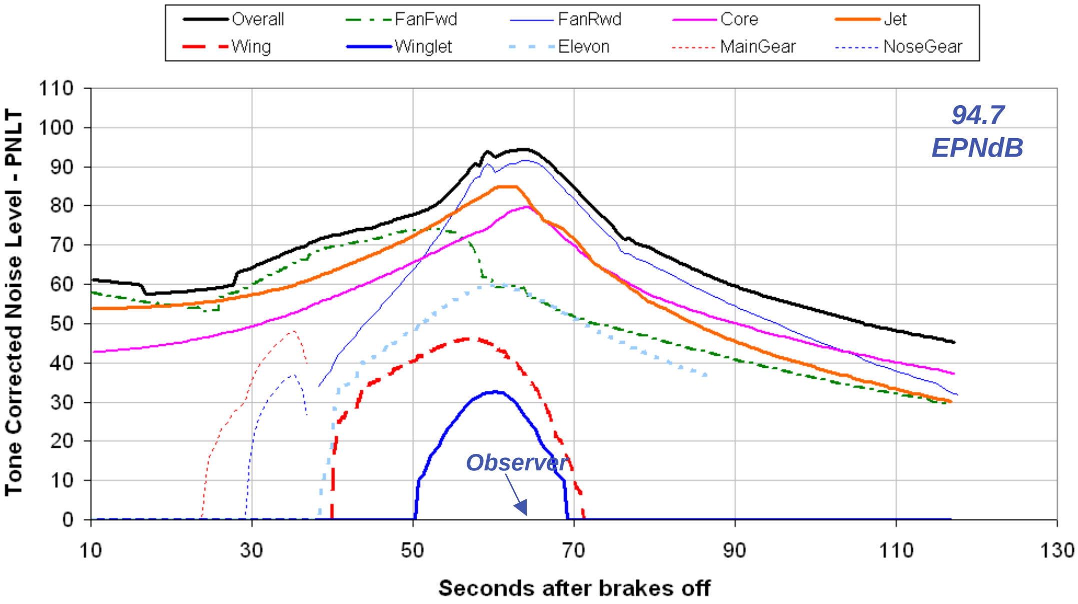

Figure 2-11: Preliminary N2B lateral PNLT and EPNL estimates[a]

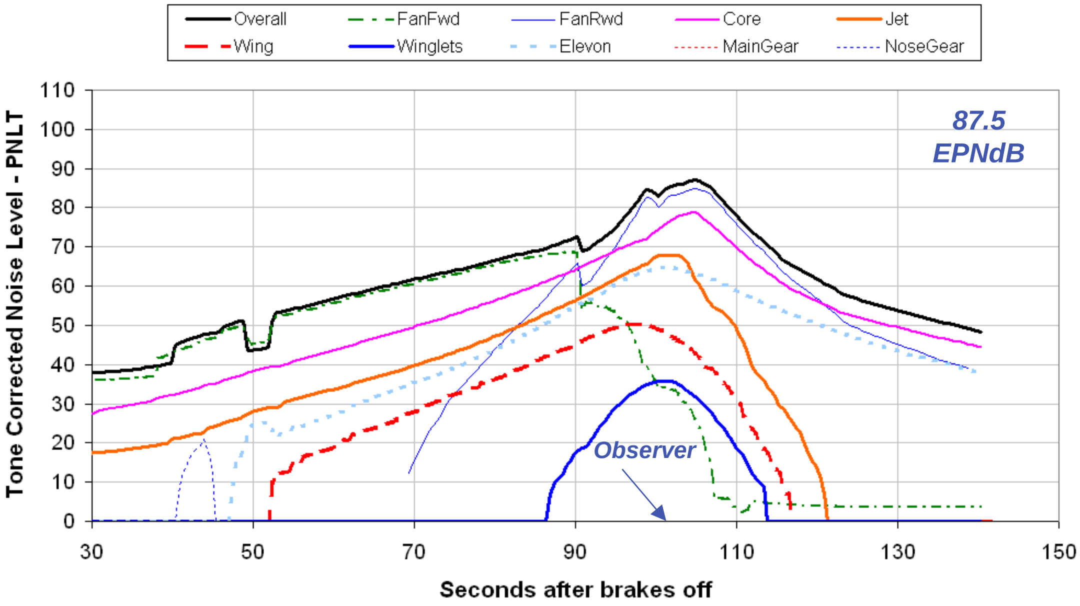

Figure 2-12: Preliminary N2B flyover PNLT and EPNL estimates[a]

---

[a] Preliminary engine noise estimates are provided for reference only and will be updated with distributed propulsion system and rectangular exhaust noise models

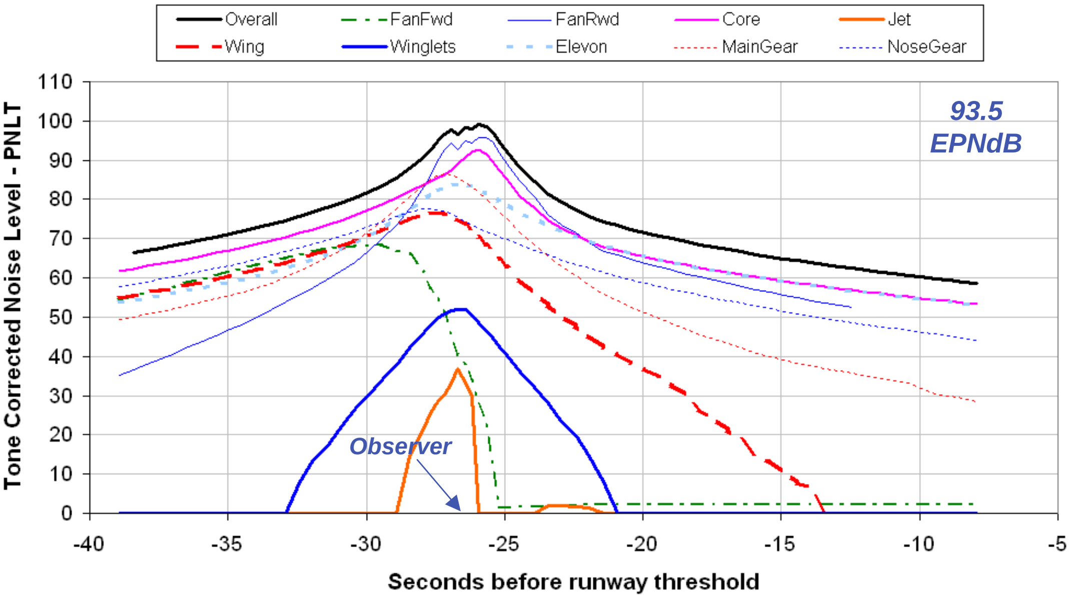

Figure 2-13: Preliminary N2B approach PNLT and EPNL estimates[a]

THIS PAGE INTENTIONALLY LEFT BLANK

Chapter 3

N2A Model–Scale Wind Tunnel Predictions

N2A scale-model wind tunnel tests are planned to evaluate airframe configurations and validate noise prediction and airframe shielding methodologies. NASA Langley Research Center's (LaRC) 14' by 22' subsonic wind tunnel is the proposed location to perform these tests. Pre-test predictions are provided here to assess the scale-model noise levels in this environment in order to set appropriate goals for the acoustic tests and allow test plan risk mitigation. As with any wind tunnel, the LaRC facility has spacial constraints on microphone array placement and when flowing there is inherent background noise due to several factors including the tunnel drive fan used to generate airflow. Therefore, the ability to measure sound pressure levels outside of the shielding shadow region and airframe noise below the wind tunnel background levels are assessed.

3.1 NASA LaRC Wind Tunnel Configuration

The setup and dimensions for the NASA LaRC Subsonic 14' x 22' wind tunnel are shown in Figure 3-1. The wind tunnel is operated in an open jet configuration that allows airflow to pass over the model while noise levels are captured with a phased microphone array outside of the jet, eliminating noise induced by flow over the mi-

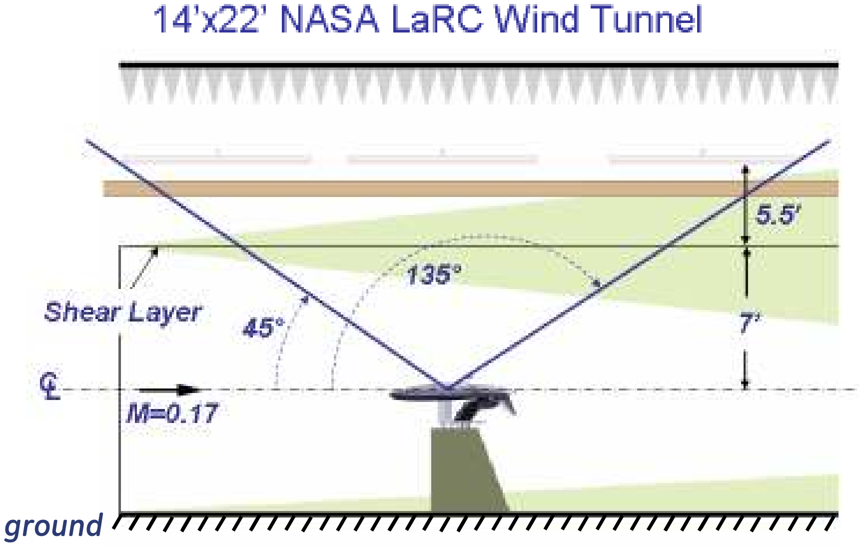

Figure 3-1: Test setup with N2A planform and engine simulator in place (picture courtesy T. Brooks - NASA [38])

crophones. However, additional background noise is generated by the shear layer due to the turbulent eddies created at the interface between the jet and the still air. In addition, the shear layer alters the measured sound pressure level of the noise source and the apparent directivity angle at the microphone location. These refraction effects are accounted for analytically and discussed below. Shear layer spreading and impingement on the microphone array in the rearward direction ultimately limit the directivity angle extent that can be recorded. In the forward direction, directivity angle is limited by the wind tunnel nozzle lip. The geometric constraints on out-of-flow measurement using the microphone array is denoted by the $45\,^\circ - 135\,^\circ$ lines.

The facility uses the Deconvolution Approach for the Mapping of Acoustic Sources (DAMAS) to post-process the measured sound pressure levels. DAMAS technology [39][40] uses a system of linear equations to remove beamforming characteristics from the captured data and allows the noise source to be more precisely mapped. The result is that specific sound contributions, such as the main strut on a landing gear or the aileron side edge, can be quantitatively assessed. This method is an improvement over standard phased array beamforming techniques that are able to capture the overall amplitude and spherical spreading of the noise source, but lack the abil-

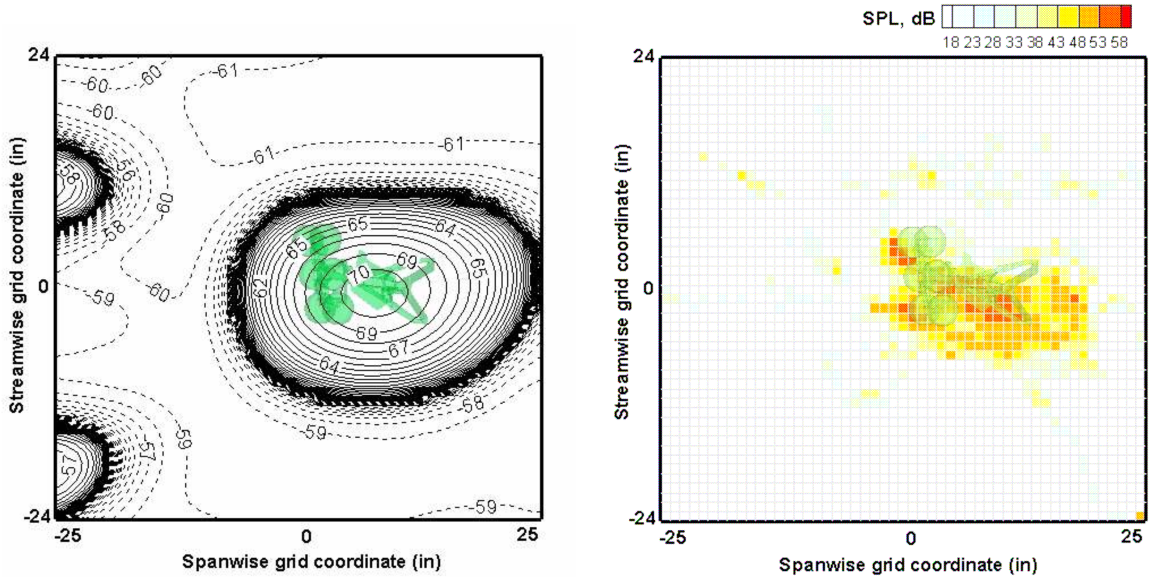

Figure 3-2: Comparison of beamforming contours (left) and DAMAS presentation (right) of 6.3% scale model 777 landing gear sound pressure levels [40]

ity to map the distribution. This is illustrated in Figure 3-2 for scale-model landing gear data obtained by Humphreys and Brooks who developed the DAMAS technique. This technique can be used for 2-D and 3-D mapping; however, array size and computational time limit the frequency levels that can be assessed.

3.2 Acoustic Scaling Assumptions

The N2A assessment discussed in Chapter 2 was scaled to estimate the model-scale noise levels in the LaRC wind tunnel. The following assumptions were made:

- Frequency and SPL are adjusted to 5.8% model-scale
- Standard day conditions are used for atmospheric attenuation
- Main landing gear fairings are not included in the noise estimates
- The shear layer is modeled as an infinitely thin vortex sheet
- All noise sources originate from the free jet centerline
- The static temperature is uniform across the shear layer

The N2A component noise hemispheres were first adjusted to model-scale before propagating them analytically to the microphone array. The acoustic energy decreases with the surface area of the noise source in the same way that energy density decreases with spherical spreading; therefore, the sound pressure level decreases by $20 \cdot \log(1/5.8\%)$. In addition, for constant reduced frequency, $\omega L/V_\infty$, the frequency of the source increases by 1/5.8%. The noise hemispheres are then propagated to the shear layer accounting for atmospheric attenuation, which becomes significant at high frequencies (above 20 kHz). The full scale 1/3-octave frequency bands under consideration extent to 10 kHz, where atmospheric attenuation is less than 0.2dB per meter; however, at the model-scale frequency of 172.4 kHz the attenuation is greater than 3dB per meter.

3.3 Shear Layer Refraction Effects

The noise hemispheres are then modified for refraction effects as the acoustic waves pass through the wind tunnel jet shear layer and then propagated to the phased array locations. The wave refraction across the shear layer changes the apparent propagation angle from the source to the observer. The angle through which the acoustic ray is refracted is calculated using Snell's law of refraction[1]. In addition, the difference in airspeed inside and outside the shear layer changes the apparent source to microphone angle and SPL. A method from Soderman and Allen [42], summarized below, is used for this calculation that accounts not only for the shear layer refraction effects but also for the noise propagation angle due to the wind tunnel airflow.

The wave emission angle in still air, $\theta^{'}$, and the shear layer to microphone angle, θ_o, are calculated by simultaneously solving the following equations,

$$M_\infty = \frac{1}{\cos\theta'} - \frac{1}{\cos\theta_o} \tag{3.1}$$

$$\theta = \tan\left(\frac{\sin\theta^{'}}{\cos\theta' - M}\right) \tag{3.2}$$

---

[1] Snell's law of refraction states that $\sin\theta_o/\sin\theta_t = v_o/v_t$, where θ is the incidence angle and v is the fluid velocity. [41]

where M_∞ is the free jet Mach number, and θ is the wave emission angle with Doppler refraction included. The mean square acoustic pressure at the microphone location is then,

$$p_{mic}^2 = p_{SL}^2 \left(\frac{\rho_o}{\rho_t D_t^{-4}} \right) \left(\frac{R^{'2}}{R_o R_a} \right) \tag{3.3}$$

where p_{SL}^2 is the acoustic pressure at the shear layer, D_t is the Doppler factor, ρ_o is the density outside the shear layer, and ρ_t is the density inside the free jet. The acoustic pressure at the microphone location is also a function of the wave emission radius in still air to the shear layer, $R^{'}$, the radius from the apparent noise source to the microphone location,

$$R_a = R_o + \left(\frac{R_t}{\sin\theta_o} \right) \left[\left(\frac{\cot\theta^{'}}{\cot\theta_o} \right)^3 - 1 \right] \tag{3.4}$$

and the distance from the free jet centerline to the microphone location along the apparent noise source radius,

$$R_o = R_m \left(\frac{\sin\theta_m}{\sin\theta_o} \right) \tag{3.5}$$

R_t is the free jet radius, R_m is the radius from the actual noise source to microphone location after shear layer refraction, and θ_m is the angle from the free jet centerline to R_m. The SPL observed at the microphone location is calculated as,

$$SPL_{mic} = SPL_{SL} + 20\log\left(\frac{p_{mic}^2}{p_{SL}^2} \right) - \alpha_f R_s \tag{3.6}$$

where SPL_{SL} is at the shear layer, α_f is the atmospheric attenuation, and R_s is the radius from the shear layer to the microphone location along the apparent noise source radius.

3.4 Pre–Test Predictions

The initial assessment suggests that phased array measurements are restricted to the shielding shadow zone and will limit the ability to evaluate shielding with the wind tunnel operating. The edge of the shadow zone is defined where the shielded an unshielded overall sound pressure levels (OASPL) are equal. Estimated insertion losses are provided in Figure 3-3. The OASPL for the turbomachinery and jet noise below are estimated based on the N2A engine architecture. Impinging jets, for the turbomachinery, and a jet simulator will be the actual noise sources in the wind tunnel test. However, Figure 3-4 illustrates that refraction has a minimal effect in the available measurement region. There is less than 1dB impact from $45\,^\circ - 135\,^\circ$. However, at large directivity angles the degree of refraction is more significant.

Estimated airframe SPL spectra at $90\,^\circ$ directivity angle together with the approximate background noise level are shown in Figure 3-5. The background noise level estimate is based on measurements with out-of-flow microphones during a UH-1 (U.S. Army Utility Helicopter) test in 1985 [43]. All airframe sources are estimated below historic wind tunnel background noise levels. The estimated airframe sound pressure levels are at least 25 dB quieter than background noise with the exception of the main landing gear. DAMAS technology allows noise to be measured at 10-15 dB below the background noise levels [40][44] that may make it possible to measure the main landing gear noise while other airframe noise sources will be a greater challenge. However, it is likely that acoustic treatment improvements have been made that will significantly reduce the background levels. This will be considered when deciding which noise sources should be targeted during this testing, the elevons in particular.

Noise levels at angles off vertical will be even more challenging to assess. Figure 3-6 illustrates the directivity effect on SPL insertion loss. Fan forward and rearward estimated noise levels decrease 20 dB off vertical and insertion effects lower the noise estimates as much as an additional 40 dB at high frequencies. The jet noise is least affected and shielding levels are approximately 10 dB. The deep shielding levels at high frequencies may be difficult to measure below background noise levels.

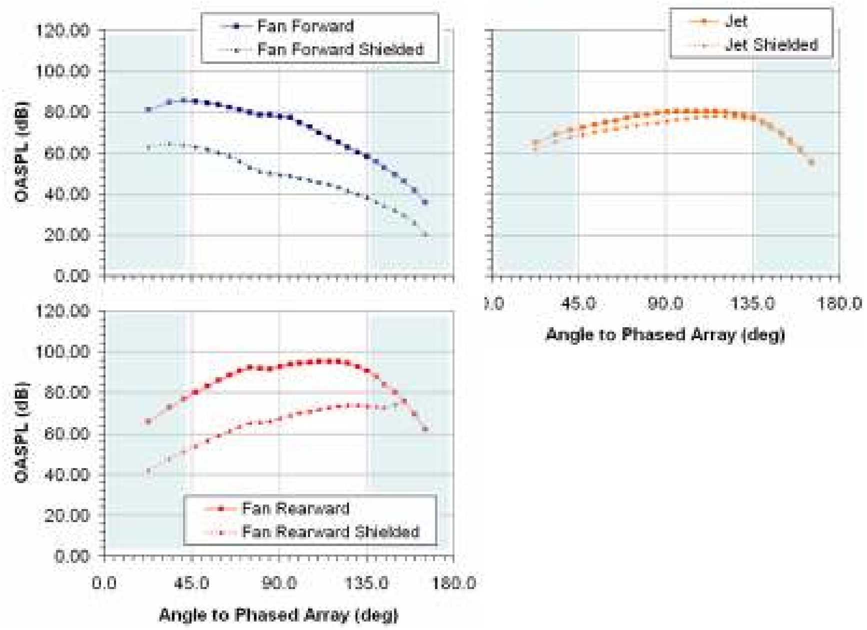

Figure 3-3: Shielded and unshielded engine noise source predictions (model scale)

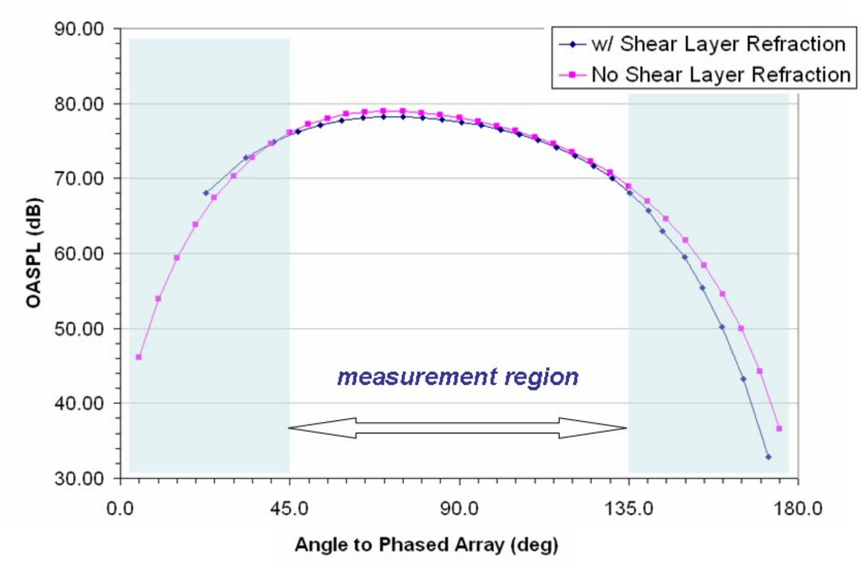

Figure 3-4: Wind tunnel shear layer refraction

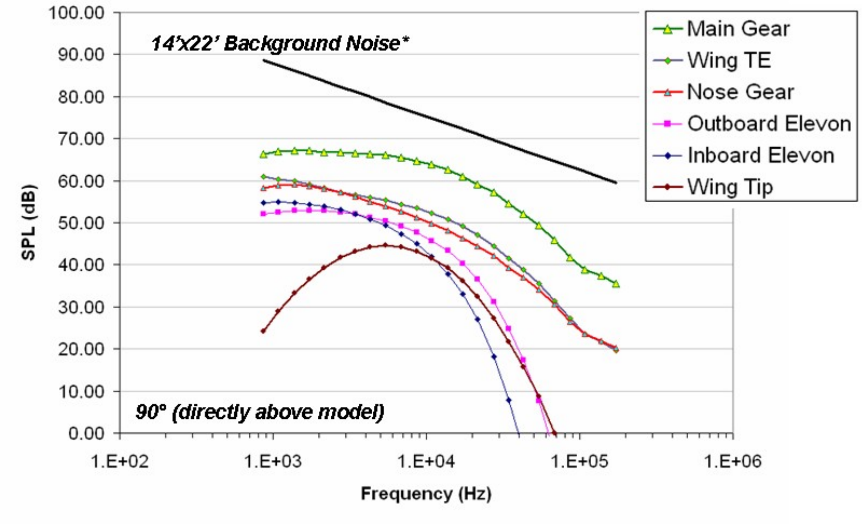

Figure 3-5: Predicted scale model SPL vs. frequency at 90 ° directivity angle with wind tunnel background noise

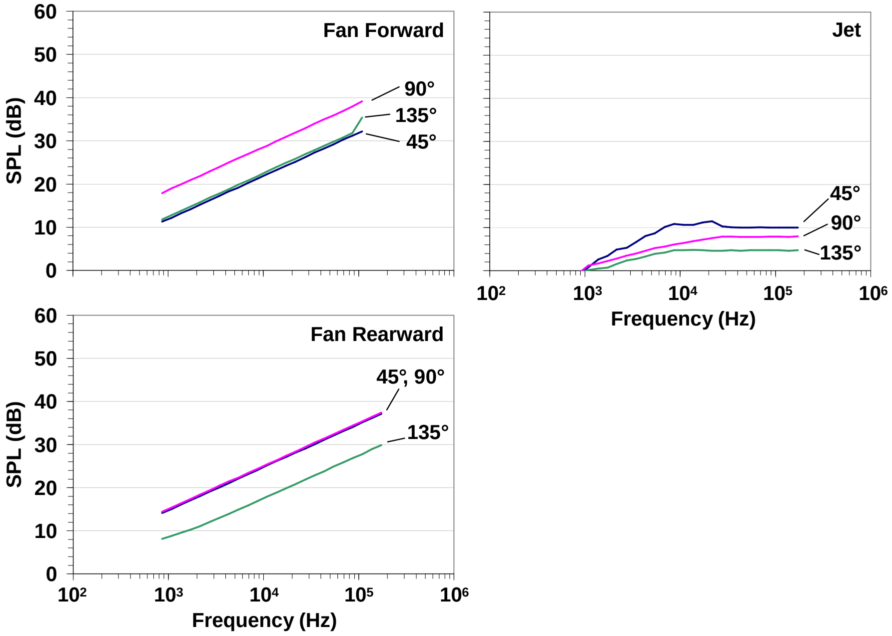

Figure 3-6: Fan forward, fan rearward, and jet shielding at 45 °, 90 °, and 135 ° directivity angles

United Technologies Research Center (UTRC) completed a similar shielding assessment for the four impinging jets that will be used to simulate turbomachinery noise sources [45]. The study showed that not only will the shielding levels at high frequency be difficult to measure below background levels, but also the impingement jet source is not omni-directional. Therefore, directionality effects will need to be incorporated into the shielding methodology to validate model results. In addition, testing with a discrete frequency point source at static conditions was recommended due to tonal interference expected with the point source that may not occur with a broadband source. The assessment also took the FAR Part 36 results from Chapter 2 and mapped the observed noise in the time domain to the wind tunnel microphone arrays. This allows the array to be positioned such that the locations match the observer times on the ground.

3.5 Summary of Results

Model scale noise estimates of the N2A aircraft configuration show that the main landing gear is 10 dB below the historical wind tunnel background noise at 10 kHz and should thus be measurable using DAMAS technology. Background noise levels may need to be lowered for other noise sources to be measurable. The elevons are a particular source of interest but require noise measurement 30 dB below background wind tunnel levels, which may be outside DAMAS capability. In addition, the phased array position constraint may be inside the shielding shadow region, which will make evaluating the planform shielding effects more challenging.

3.6 Conclusions and Recommendations

Shielding measurements may have to be completed with a no-flow test. A no-flow test allows the microphone array to be positioned forward and aft of the model to measure a wider directivity angle range and eliminates the wind tunnel background noise. It also eliminates the shear layer diffraction impact that limits the directivity angle in the aft direction.

Additional care should be taken to reduce background noise levels to enable the detection of other airframe noise sources during the wind tunnel test. Wing trailing edge and nose landing gear noise sources are estimated at about 25 dB below background noise. The elevon noise level may be an additional 5 dB or more lower. Finally, at an estimate 40 dB below background noise levels, wingtip noise levels measurement may be difficult.

Chapter 4

N2B Propulsion System Integration

Embedding the N2B propulsion system in the airframe not only provides noise shielding, but it also has the potential to reduce fuel burn by ingesting the airframe boundary layer. To understand how BLI improves performance, first consider an aircraft with podded engines, such as the N2A. In general, the engines that are producing thrust can be analytically separated from the airframe that is generating drag because their flow fields are not aerodynamically coupled. The engines accelerate free stream air to produce thrust (net momentum surplus) that balances the airframe drag (net momentum deficit) for steady level flight. This leads to excess kinetic energy in the wake downstream of the engine. This is relevant as propulsive efficiency is the ratio of propulsive power (thrust x free stream velocity) to the mechanical power input to the airflow (rate of kinetic energy production). Alternatively, BLI engines accelerate the lower momentum flow of the airframe boundary layer to near free stream conditions thereby reducing wasted kinetic energy and increasing propulsive efficiency relative to podded engines. In the idealized 100% BLI case, the entire airframe momentum deficit is 'filled in' by the propulsion system requiring no excess kinetic energy. However, BLI propulsion systems not only present analytical and modeling challenges, but also pose significant technological challenges and associated risks in the development of inlet distortion tolerant fan designs.

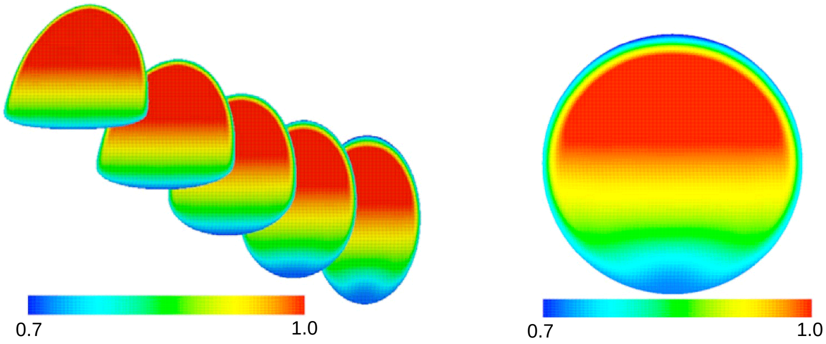

Figure 4-1: Normalized stagnation pressure profile (P_t/P_∞ for the SAX-40 inlet)[12]

One analytical challenge is that thrust and drag are not easily separated in highly integrated propulsion systems and performance accounting becomes complicated. The wake momentum deficit decreases as the amount of BLI increases and the thrust required is not constant. Therefore, conventional parameters such as specific fuel consumption (SFC) that define fuel burn using net thrust are not practical as metrics in the design optimization. Engine mechanical power required is a more useful metric because it is directly proportional to fuel power through thermal efficiency and minimizing it will minimize fuel burn. The power required is calculated by balancing power sources and sinks in the Trefftz plane[1] downstream of the aircraft, using methods developed by Drela[46] and Giles and Cummings[47]. This eliminates the need to separate thrust and drag. This process is described in greater detail in Sections 4.2 and 4.4.

Inlet distortion is a design risk that accompanies the BLI performance benefit as the airframe boundary layer generates a reduced total pressure region in the inlet. This is shown in Figure 4-1 for a SAX-40 candidate inlet design at several locations in the S-duct and at the fan face. Inlet total pressure distortion reduces fan stall margin relative to a clean inlet profile and the forced response of the blade to the non-uniform pressure profile poses an aeromechanical risk. Therefore, a distortion tolerant fan design is required to insure stall free operation and blade structural integrity.

---

[1] The Trefftz plane is defined as the location downstream of the aircraft where the flow has returned to free stream static pressure.

However, it is possible to mitigate these design risks by reducing the boundary layer thickness and the associated distortion content.

The integral nature of the BLI engine is such that fan inlet conditions, fan face Mach number, and the state of the airframe boundary layer are coupled. The fan operating conditions govern the pre-compression or diffusion of the flow upstream of the inlet. As such, higher fan face Mach numbers tend to alleviate the diffusion by the airframe and thus favorably affect the boundary layer properties and state, potentially mitigating inlet distortion and decreasing lost propulsive power. This will be discussed in more detail in Section 4.2. The design trade is that increased fan face Mach numbers lead to increased fan losses. The question arises whether a balance can be struck between improving propulsive power consumption and mitigating inlet distortion to reduce the overall risk of BLI. This chapter presents a study which hypothesizes that an optimum fan face Mach number exists that minimizes inlet distortion while maximizing the BLI performance benefit as illustrated schematically in Figure 4-2.

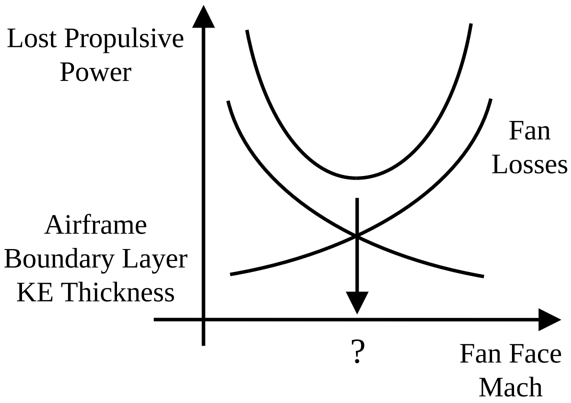

Figure 4-2: Hypothesis: Optimum fan face Mach number minimizes lost propulsive power

4.1 Previous Research

Past research has quantified the BLI performance improvement of aircraft, marine applications, and more recently embedded turbofan engines. Smith [48] investigated BLI effects on unducted propulsors situated in the aircraft wake with purely radial inlet distortion. The analysis recognized the aforementioned need for a metric to track performance improvement in integrated propulsion systems and first proposed the Power Savings Coefficient (PSC). The PSC compares the propulsive power required for steady level flight of a BLI system to that of a baseline non-BLI system,

$$PSC = \frac{P_P' - P_P}{V_o D / \eta_P'} \tag{4.1}$$

where P_P is propulsive power, V_o is the flight velocity, D is drag, η_P is propulsive efficiency and $'$ indicate the non-BLI case. The research assumed a constant inlet static pressure while emphasizing that the impact of the propulsor on the upstream flow, known as field effects, are important and need to be understood for actual implementation. BLI power savings of 20% were shown noting that boundary layers nearest separation and propulsors that most effectively flattened the wake deficit (wake recovery or distortion transfer) had the largest benefit. The potential field effects along with flow field impact on fan performance were recognized but not quantified in this analysis.

Plas et al. [12] investigated the impact of BLI on fan performance for the SAX-40 using several modeling techniques. A major focus of this research was to model the amount of distortion transfer across the fan and related performance improvement. A 1-D inviscid parallel compressor model for a straight duct showed a linear increase in power savings with percent of ingested boundary layer. A 2-D straight duct integrated boundary layer analysis confirmed that power savings increases with distortion attenuation across the fan. The 3-D inviscid fan body force model is the most complete, calculating the distortion transfer across the fan based on inlet conditions from a separate airframe CFD analysis. Power savings of 3-4% are estimated assuming constant airframe drag and using a constant fan diameter.

Sargeant [49] proposed a method to analytically separate the engine and airframe control volumes. Boundary layer flow is allowed to return to free stream pressure using the Von Karman integral equation along an inviscid surface and the propulsor is taken to act behind the aircraft. This methodology simplified the field effects mentioned by Smith. Including propulsive efficiency benefits, drag reduction, and engine performance penalties resulted in an estimated 4.9% power savings compared to podded engines. Engine effect on upstream flow over the aircraft body was also investigated; however, the interaction between the engine inlet conditions, fan face Mach number, and the overall system performance were not considered.

4.2 Power Balance Methodology

Drela [46] provides a power-based methodology that eliminates the need to separate thrust and drag. Instead, energy outflow, $\dot{E}$, and viscous dissipation, Φ, are balanced at the Trefftz plane by mechanical power sources, P.

$$P = \dot{E}_a + \dot{E}_v + \Phi_{surface} + \Phi_{jet} + \Phi_{wake} + \Phi_{vortex} + \Phi_{shock} \tag{4.2}$$

Axial kinetic energy deposition, $\dot{E}_a$, is the result of both velocity excess in jets and deficit in wakes. A lift induced vortex wake (induced drag in a momentum balance) is a source of transverse kinetic energy deposition, $\dot{E}_v$. The viscous dissipations are when kinetic energy is irreversibly converted to heat. These processes occur in surface boundary layers, $\Phi_{surface}$, downstream in free shear layers, Φ_{jet} and Φ_{wake}, and free vortices, Φ_{vortex}. In the case where supersonic flow exists, shock formation is an additional irreversible process, Φ_{shock}. The benefit of BLI comes from minimizing or eliminating $\dot{E}_a$, Φ_{jet}, and Φ_{wake} by using lower momentum flow to propel the aircraft.

Drela uses this methodology to derive power savings for a transonic airfoil. Figure 4-3 illustrates the difference in viscous dissipation, Φ, between two idealized systems. The power requirement is the sum of the surface and wake losses in the isolated propulsor case. In contrast, the BLI power balance requires only the surface

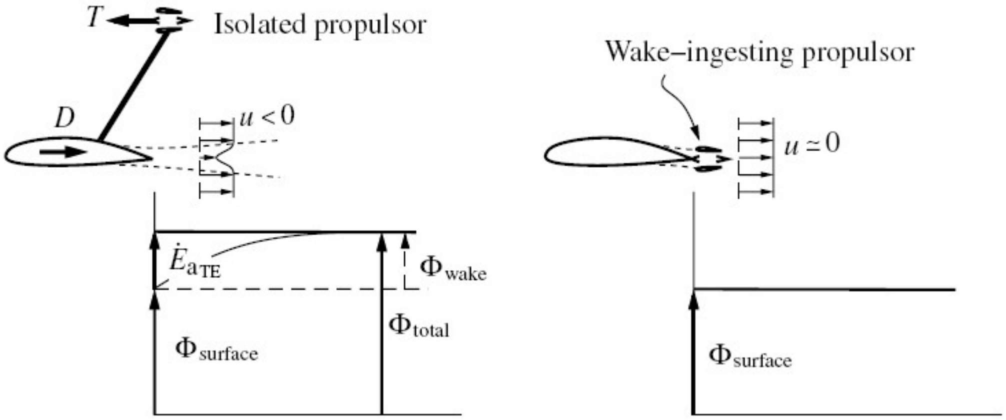

Figure 4-3: Comparison of dissipation in an isolated (podded) and 100% wake-ingesting (embedded) propulsors [46]

dissipation contribution. Kinetic energy thickness, θ^*, characterizes the total viscous dissipation at all locations along the flow path,

$$\theta^* = \int_0^{y_e} \left(1 - \frac{u_x^2}{u_e^2}\right) \frac{\rho u_x}{\rho_e u_e} \, \mathrm{d}y \tag{4.3}$$

$$\Phi(x) = \frac{1}{2} \rho_e u_e^3 \theta^*(x) = \int_0^x \rho_e u_e^3 C_D \, \mathrm{d}x \tag{4.4}$$

where u is velocity, ρ is density, x is the axial distance from the airfoil leading edge, y is radial location perpendicular to the flow, C_D is the viscous dissipation coefficient, and e denotes a boundary layer edge quantity. 2-D viscous CFD reveals that wake dissipation contributes 13% of lost work to the flow and 100% BLI would realize this power savings.

4.3 Two-Dimensional Modeling Approach

The previous work discussed above reiterates and quantifies the significant power savings potential of BLI propulsion systems at the expense of elevated inlet distortion levels. The studies also suggest that both the airframe and the engine should be included in one model to determine the impact of fan inlet conditions on the boundary layer properties and the power savings. However, modeling the entire system becomes

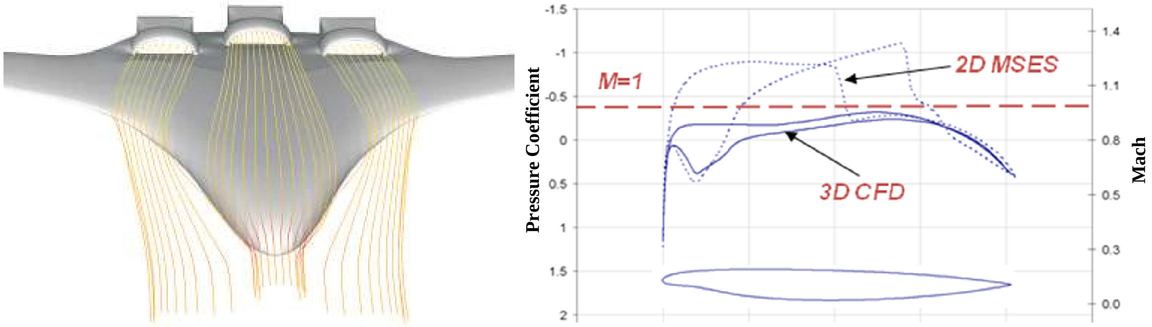

Figure 4-4: (left) Panel method computation [49] illustrates 3-D effects and (right) 2-D pressure coefficient computations of centerbody profile compared to 3-D results

computationally expensive and limits the ability to explore the design space parametrically. The system is therefore reduced to a 2-D model for the following parametric study.

Although a 2-D study is desired, the flow around the aircraft centerbody is inherently 3-D and thus the model has limitations. Spanwise flow around the centerbody relieves transonic stressing of the airframe suction surface and in the case of the N2B maintains subsonic flow. This is illustrated in Figure 4-4 (left) where Sargeant investigated the flow characteristics of the SAX-40 aircraft using a 3-D panel method calculation [49]. The figure also shows the streamtubes captured by each of the nacelles at cruise.

Figure 4-4 (right) compares the Mach number and pressure coefficient, C_p, distributions of the centerbody with and without the 3-D relief effects. These effects must be adequately represented in the 2-D calculation. The method used here is to model the relief as an internal flow calculation inside a 2-D channel with tailored inviscid walls replicating the pressure distribution along the 3-D centerbody, as shown in Figure 4-5.

The resulting 2-D model of the 3-D flow has slight pressure differences near the leading edge and along the pressure side of the centerbody, illustrated in Figure 4-6. However, the purpose of this investigation is to determine the sensitivity of fan inlet conditions on the flow over the suction surface of the centerbody. Sargeant [49] determined in his studies that flow more than 3.33 fan diameters upstream of the inlet

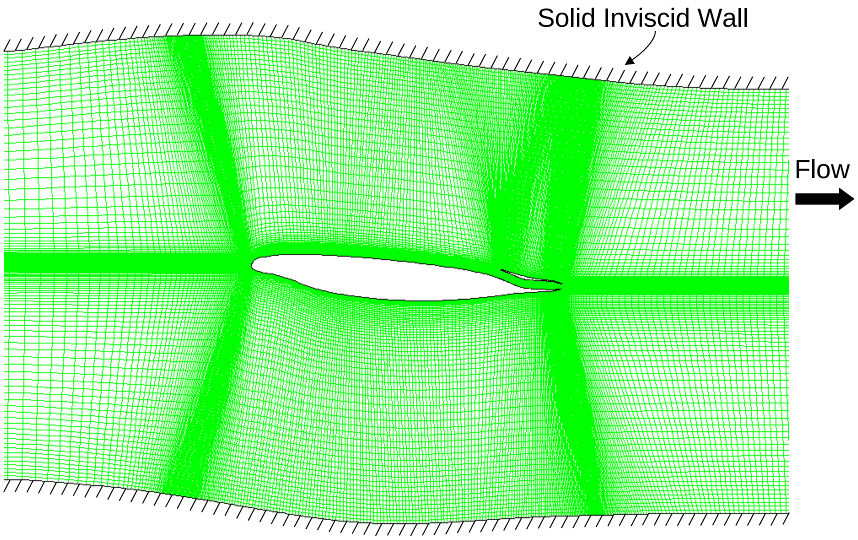

Figure 4-5: Grid showing 2-D approach to 3-D BLI problem. Top and bottom faces are solid inviscid surfaces (only partial domain is shown)

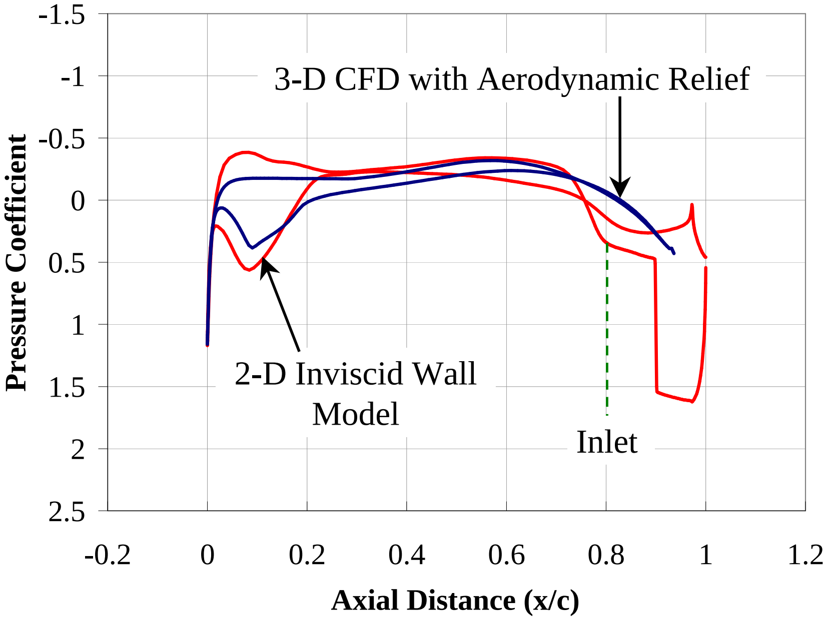

Figure 4-6: 2-D viscous CFD computation of centerbody pressure distribution with powered nacelle (red) compared with solution from 3-D viscous CFD calculation (blue)

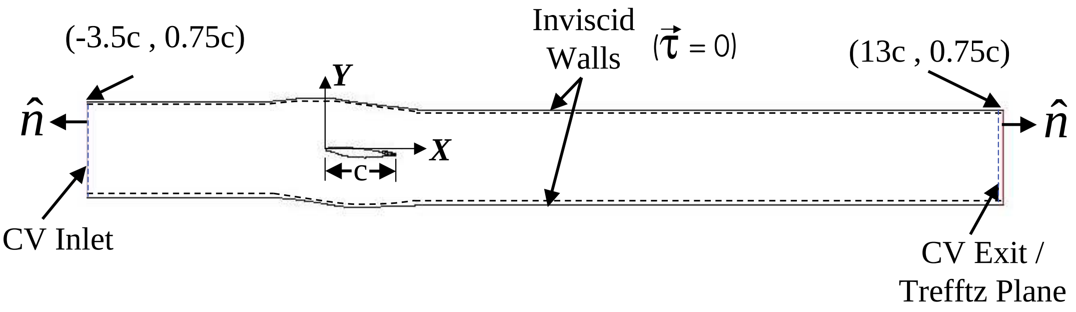

Figure 4-7: 2-D control volume for Trefftz plane power balance

is not affected by the fan and the 2-D inviscid wall model shows good agreement to the 3-D CFD beyond 25% chord. In addition, pre-compression[2] begins approximately 2.7 fan diameters ahead of the inlet and C_p increases to 0.5 at the fan face. This shows reasonable agreement to Sargeant's results where C_p increased to 0.7 at the inlet. Therefore, inviscid walls are sufficient to model the 3-D relief.

The impact of the pre-compression on the boundary layer properties is also important for testing the stated hypothesis. Therefore, a rigorous grid sensitivity study was conducted to insure adequate cell density[3] near the airfoil surface while minimizing convergence time. Model convergence time is constrained in this investigation to allow parametric analyses to be completed quickly for design optimization. The resulting structured grid has approximately 88000 cells extending 3.5 and 12 chord lengths upstream and downstream, respectively, as depicted in Figure 4-7. The extension of the downstream domain enables a power balance in the Trefftz plane.

The $\kappa - \omega$ shear-stress transport (SST) turbulence model is chosen for this analysis. The impact of fan face Mach number on airframe boundary layer properties and fan distortion transfer to the downstream flow field in this analysis is the main consideration in choosing this turbulent model.

---

[2] Ideally, all of the flow diffusion (pre-compression) should be done outside of the nacelle for the best inlet pressure recovery.

[3] The airfoil adjacent cell dimensionless wall distance (y^+) was generally kept between $30 - 300$, per FLUENT software guidelines, with no values larger than 500

The $\kappa - \omega$ SST model has demonstrated close agreement with measurements for far wakes and jets and can be used for external and free shear flows [50].

4.3.1 Fan Body Force Model

A fan model is also included in the 2-D analysis using an actuator volume representation, shown in Figure 4-8, where stagnation pressure and temperature rise across the fan stage, including aerodynamic loss effects, are implemented via source terms using FLUENT software. These additional source terms, referred to as body forces, represent the fan blade row aerodynamic loads and eliminate the need to model the 3-D blade geometry. Instead, the momentum and energy equations are modified using a FLUENT software User Defined Function (UDF). This approach allows for radial streamline shifts through the fan stage and thus captures the distortion transfer, simplified here in the 2-D analysis as a radial inlet flow distortion. The block diagram in Figure 4-9 illustrates the overall process and is explained in detail below.

The design point fan stage pressure ratio is input to the momentum equation as a body force acting on the fluid to impart a total pressure rise across the actuator volume. For steady flow, the momentum equation is,

$$\nabla \cdot (\rho \overrightarrow{v} \overrightarrow{v}) = -\nabla p + \nabla \cdot \bar{\bar{\tau}} + \overrightarrow{F} \tag{4.5}$$

where ρ is density, $\overrightarrow{v}$ is the velocity vector, $\bar{\bar{\tau}}$ is the viscous stress tensor, and $\overrightarrow{F}$ is the body force vector. The resulting momentum source terms set in the FLUENT software UDF are,

$$F_x = \frac{dp}{dx} \cdot \cos\theta \quad and \quad F_y = \frac{dp}{dx} \cdot \sin\theta \tag{4.6}$$

where θ is the flow angle, x is in the axial direction, and y is in the radial direction.

Source terms are also added to the energy equation which represent the work done by the fan and the resulting stagnation temperature rise. For steady adiabatic flow the energy equation can be written as,

$$\nabla \cdot (\rho h_o \overrightarrow{v}) = \nabla \cdot (\bar{\bar{\tau}}) + S_h \tag{4.7}$$

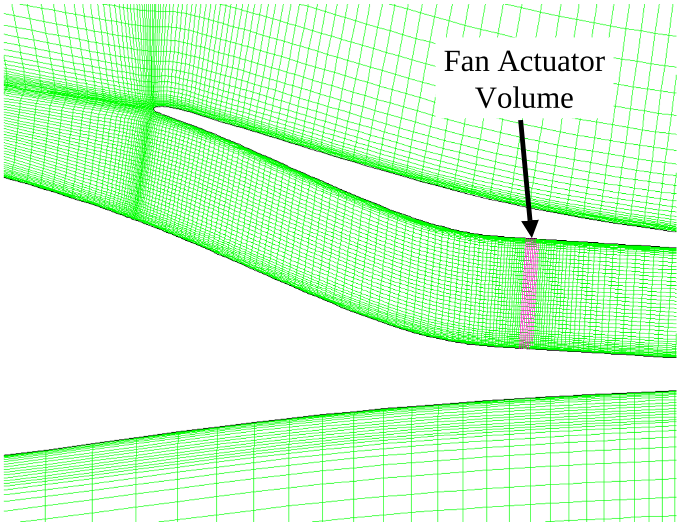

Figure 4-8: 2-D actuator volume grid

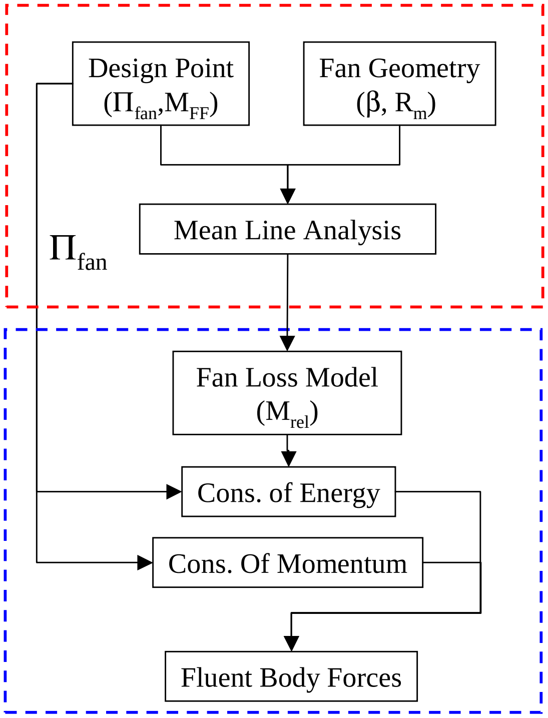

Figure 4-9: Flow diagram for fan model calculations completed external (Top) and internal (Bottom) to FLUENT software

where h_o is stagnation enthalpy and S_h is the body force term. The stagnation enthalpy rise across a slice of thickness dx of the actuator volume,

$$dh_o = c_p dT_o \tag{4.8}$$

is rewritten using the definition of adiabatic efficiency and isentropic relations to determine the body force source term in the energy equation,

$$S_h = \frac{\rho v c_p T_{o1}}{dx}\left(\frac{1}{\eta_f}\left(\pi_f^{\frac{\gamma-1}{\gamma}} - 1\right)\right) \tag{4.9}$$

where T_o is the stagnation temperature, c_p is the specific heat at constant pressure, η_f is the fan efficiency, π_f is the fan total pressure ratio, γ is the ratio of specific heats, and T_{o1} is the total temperature upstream of the actuator volume.

The fan relative Mach number, which is a function of fan rotor speed, is required to determine the fan adiabatic efficiency in the energy source term. A 1-D mean-line velocity triangle analysis, depicted in Figure 4-10, is conducted to determine the rotor speed, which is dictated by the fan stage geometry and the design point performance chosen above. This is completed as a preprocessing step to the FLUENT software UDF, using the Euler turbomachinery equation to relate the stagnation enthalpy increase of the fluid to the shaft work input by the fan and the resulting change in angular momentum.

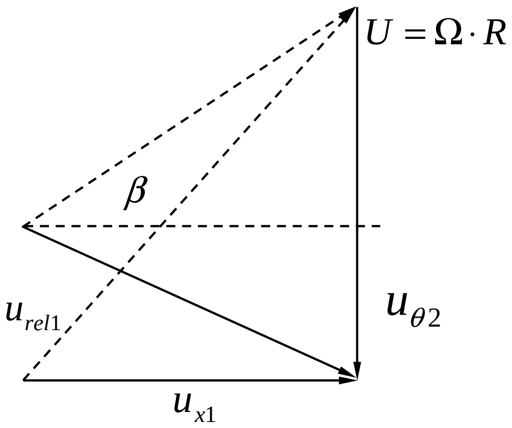

Figure 4-10: Fan meanline velocity triangle

If there are no inlet guide vanes and axial velocity is constant, the meanline relationship is

$$dh_o = \Omega R_m u_{\theta 2} \tag{4.10}$$

where Ω is the fan speed, R_m is the meanline radius, and $u_{\theta 2}$ is the exit tangential velocity. The velocity triangle is used to find,

$$u_{\theta 2} = \Omega R_m - u_x \tan \beta \tag{4.11}$$

where u_x is the axial velocity and β is the trailing edge metal angle, set to 35 ° based on the Granta engine design [51]. The fan speed is input to the UDF fan model and relative velocity and Mach number are calculated along the fan to determine the overall efficiency loss as described below.

4.3.2 Fan Loss Model

To capture the impact of fan face Mach number on fan performance the body force model must respond to the inlet flow conditions. This is accomplished by using fan loss models based on first principles that scale with relative Mach number. The models are summarized in Table 4.1 and described below.

Table 4.1: Fan loss sources and UDF assumptions

Fan Loss Sources	Model Scaling and Assumptions	Source
Profile Loss	$\sim (M_{rel}^3)$	Denton[52]
Shock Loss	$\sim (M_{rel}^2 - 1)^3$	
Wake Mixing Loss	20% of profile loss	Hall[53] and Denton[52]
Endwall Loss	1 pt	
Tip Leakage Loss	1 pt for 1% gap/span	
Inlet Distortion (BLI)	1 pt	Reid[54]

Nearly 50% of the fan lost work is due to boundary layer dissipation, or profile loss. This source of entropy generation is calculated by integrating the dissipation along the surface of the blade[52],

$$T_\delta \dot{S} = \int_0^x \rho V_\delta^3 C_d \, \mathrm{d}x \tag{4.12}$$

The viscous dissipation coefficient is a function of Reynolds number; however, for turbulent flow it is relatively constant and approximately 0.002 [55][56]. The boundary layer edge velocity, V_δ, in this case is fan relative velocity,

$$u_{rel1} = \sqrt{U^2 + u_{x1}^2} \tag{4.13}$$

as set by the velocity triangle using the free stream value at each of the fan actuator volume grid locations shown in Figure 4-8.

Shock waves are another source of lost work. Entropy generation in the shock due to viscous dissipation and irreversible heat transfer scales with relative Mach number,

$$\Delta s \approx c_v \frac{2\gamma(\gamma-1)}{3(\gamma+1)^2}(M^2-1)^3 + O\left(M^2-1\right)^4 \tag{4.14}$$

where c_v is specific heat at constant volume [52]. Shock waves form at oblique angles on airfoils and therefore the Mach number normal to the shock is lower than fan relative Mach number. However, the shocks are assumed to be normal in this analysis and therefore the calculated lost work is to be viewed as a conservative estimate.

Turbulent mixing losses due to trailing edge flow separation and mixing out of the boundary layer do not lend to Mach number scaling as with profile and shock losses. This contribution is a function of shape factor and entropy thickness [52]. However, Hall [53] finds mixing losses to be approximately 20% of the profile loss for a wide range of flow and stage loading coefficients in his work on gas turbine engine efficiency limits. Therefore, variations in turbulent mixing losses based on the inlet conditions are neglected and 20% of the profile loss is assumed here.

The remaining loss contributions, endwall, tip clearance, and 3-D effects, have nearly constant performance penalties for fan operating points at cruise. Viscous shear losses in the fan endwall boundary layer are compounded by the flow around the tip of the fan blade [52]. At the design point these losses account for a 2-point loss in fan efficiency based on a 1 percent of span tip clearance [53]. Additional 3-D distortion transfer losses cannot be captured by the 2-D model and are assumed to contribute a 1-point loss for all fan face Mach numbers based on work by Reid [54].

4.4 Power Balance Analysis

With the fan model integrated into the airframe CFD model, the power balance analysis discussed in Section 4.2 is required to determine the fan pressure ratio and airflow required to balance power in the Trefftz plane. The control volume in Figure 4-7 is used for this assessment. In addition, the 3-D contributions to airframe lost power are included separately in this analysis since only the centerbody is modeled in the 2-D approach. The wake transverse kinetic energy near the wing tips (lost power due to induced drag), and the outer wing dissipation due to surface effects, wake mixing and shock loss are added to the contributions from the centerbody using Equation 4.2.

$$P_{trefftz} = \Big[\dot{E}_a + \Phi_{surface} + \Phi_{jet} + \Phi_{wake}\Big]_{Centerbody} + \cdots \\ \Big[\dot{E}_v + \Phi_{surface} + \Phi_{wake} + \Phi_{shock}\Big]_{OuterWing} \quad (4.15)$$

Quasi 3-D aerodynamic assessment tools developed by MIT as part of the Silent Aircraft Initiative were used to estimate the drag contributions of both the centerbody and outer wing sections using a 2-D inviscid vortex lattice method, 2-D viscous airfoil calculations, and empirical drag formulas. These contributions calculated for the unpowered airframe [4] are summarized in Table 4.2.

Table 4.2: 3-D airframe contributions to lost power

Source of Lost Power	Power/(Lift $\cdot V_\infty$)
Lift Induced Drag ($\dot{E}_v$)	0.0160
Outer Wing Wake Drag (Φ_{wake})	0.0025
Outer Wing Viscous Drag ($\Phi_{surface}$)	0.0072
Outer Wing Shock Wave Drag (Φ_{shock})	0.0007

The centerbody is taken to occupy the space between the outer two propulsors as shown in Figure 4-11. The wake and surface dissipation effects of the centerbody and jet dissipation of the propulsor together with the wake and jet streamwise kinetic energy deposition rate are computed from the 2-D calculations. The sum of the centerbody and outer wing power consumption and power outflow, Equation 4.15, must be balanced with the total mechanical power supplied by the propulsion system.

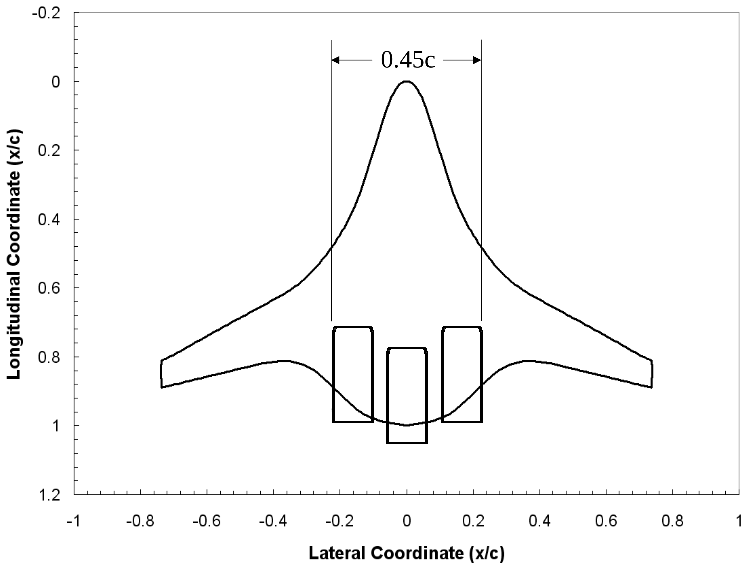

Figure 4-11: N2B geometry and centerbody assumption

The centerbody components are calculated from the control volume using Giles and Cummings wake integration method in the Trefftz plane [47]. The first integral term in Equation 4.16 captures the entropy increase due to viscous dissipation in the boundary layer and the wake from the centerbody and the nacelle, the nacelle shock loss, and the non-ideal fan losses modeled in the actuator volume. The second term inside the integral is the power provided by the engine.

$$P_{trefftz} \approx \int_{trefftz} \left(p_\infty \frac{s}{R} - \rho_\infty \Delta H \right) \cdot V \, \mathrm{d}y + \cdots$$
$$\left[\dot{E}_v + \Phi_{surface} + \Phi_{wake} + \Phi_{shock} \right]_{OuterWing} = 0 \quad (4.16)$$

4.4.1 Two-Dimensional Parametric Power Balance Study

Using the method described above, a series of balanced power conditions are developed in order to investigate how power savings is governed by changes in fan face Mach number. There are two ways to adjust the fan face Mach number at a fixed cruise condition to balance the power: either the inlet area is kept constant while varying the nozzle exhaust area (fixed nacelle, variable nozzle), or the inlet to exhaust area ratio is kept constant while changing the inlet area (fixed nacelle and nozzle shape, variable nacelle offset). Fan pressure ratio is varied in the fan actuator volume model until the power is balanced in the Trefftz plane. A block diagram in Figure 4-12 illustrates the iterative process.

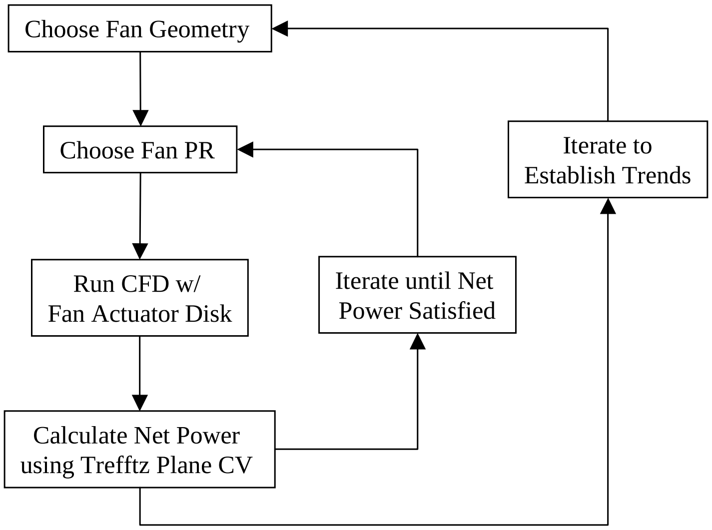

Figure 4-12: Block diagram showing design iteration process using 2-D simulations

A parametric study is carried out to find the locus of balanced power conditions at different fan operating points. Varying exhaust nozzle area ratio shifts the throttle curve left or right, while varying inlet area and keeping the area ratio constant holds the same throttle curve or operating line. This is shown in Figure 4-13 for the range of inlet areas and exhaust area ratios examined in this analysis.

The trends in the balanced power conditions can be explained using a qualitative examination of the fan corrected flow. Based on corrected flow considerations,

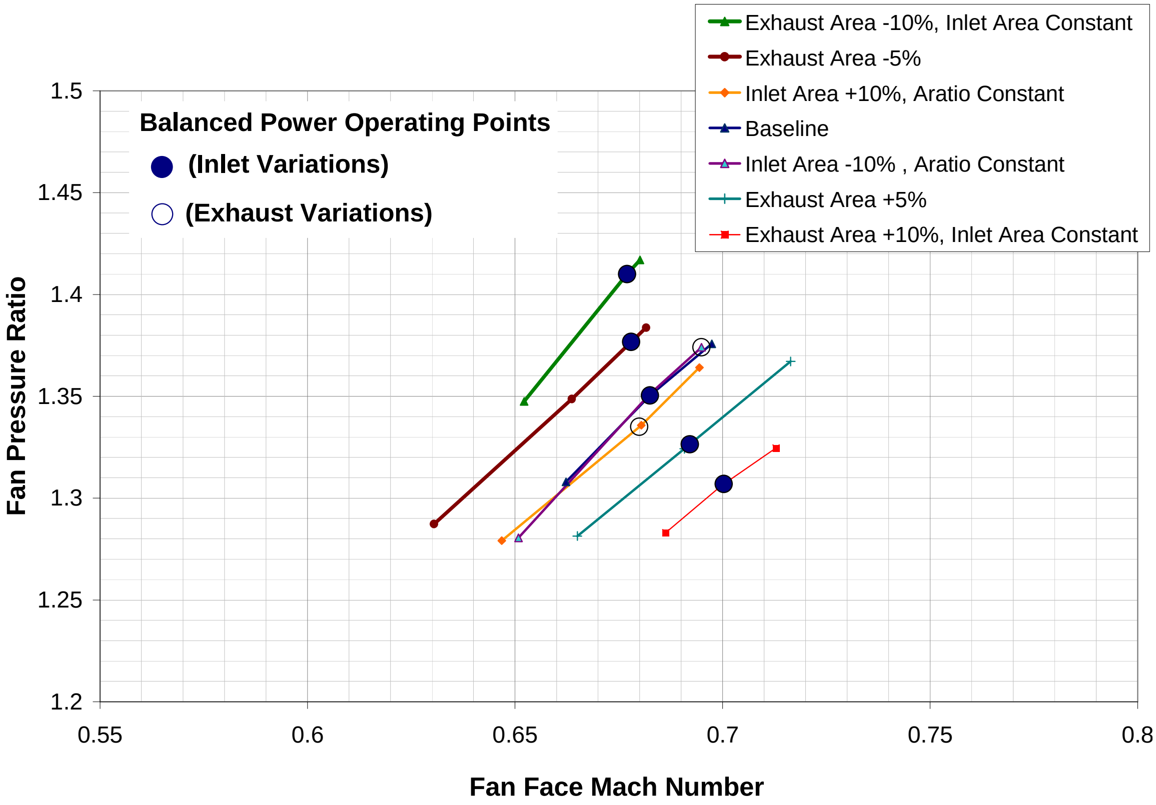

Figure 4-13: N2B balanced power operating points based on 2-D fan analysis

increasing area ratio while keeping FPR constant leads to an increase in mass flow and therefore fan face Mach number. However, to meet power balance requirements the fan pressure ratio has to be reduced such that the fan operating point shifts to higher Mach numbers and lower FPR as indicated by the solid blue circles. It will be shown in Section 4.5 that this also results in maximized power savings. If instead area ratio is held constant the operating point follows a fixed throttle curve. Mass flow increases with inlet area such that FPR must be reduced to balance power as indicated by the open blue circles.

4.4.2 Preliminary Nacelle Design

A preliminary inlet design has not been completed for the N2B; therefore, the starting point of the inlet parametric study is based on the SAX-40. The assessment of the original airframe-nacelle configuration revealed a rather large separation on the upper side of the nacelle in the 2-D calculations. The Mach number contours for the original SAX-40 based nacelle design are shown on the left in Figure 4-14. The large separation can be avoided by reshaping the nacelle suction side; however, the shock cannot be eliminated. A detailed 3-D design study is being conducted as a follow-on to this analysis where area ruling will be applied to reduce or eliminate the shock. The design shown on the right in Figure 4-10 was deemed acceptable for the integration study to be carried out here.

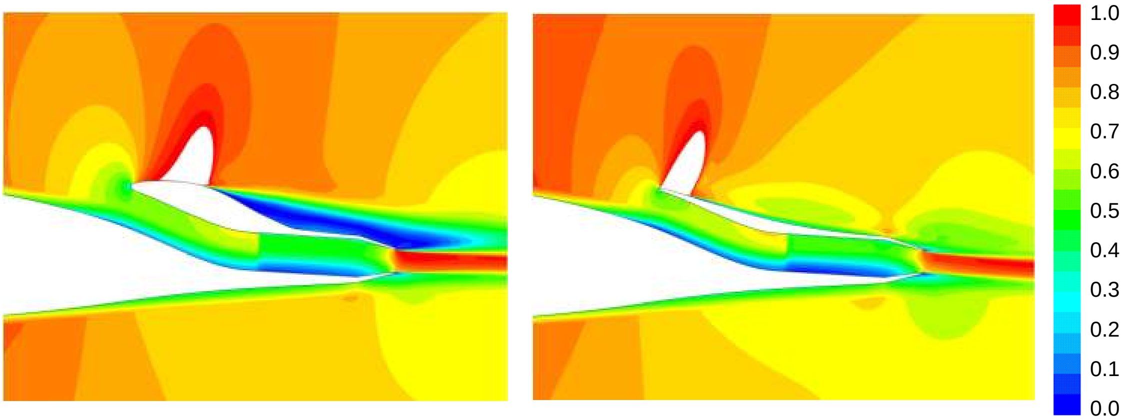

Figure 4-14: 2-D N2B nacelle assessment: Mach number contours of original SAX-40 design (left) and improved design (right)

4.5 Power Savings Trends with Fan Face Mach Number

Using the recontoured nacelle, the iterative process described in Section 4.4.1 was carried out to investigate whether an optimum fan face Mach number can be found for the N2B propulsion system. A range of exhaust nozzle area ratios and inlet areas were run to find balanced power design points in order to validate the hypothesis and trends above. The flight conditions for the analysis are Mach 0.8, 40,000 ft, and ISA $+10\,^{\circ}K$, which is the steady level cruise condition.

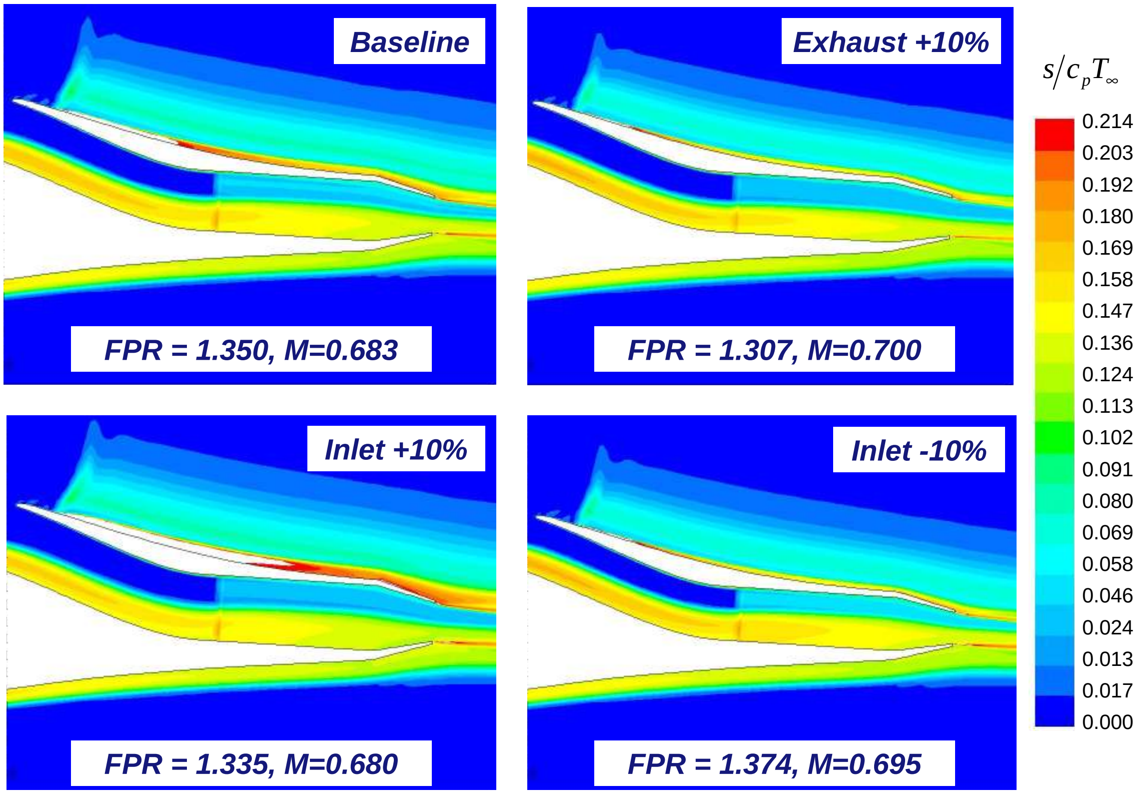

Figure 4-15: Entropy generation for several fan geometries and operating points

Entropy generation for several design points is shown above, demonstrating the model capability. The boundary layer thickness is evident and found to decrease approximately 4.7% from the baseline case to the decreased area ratio and lower fan pressure ratio case where the fan face Mach number are 0.68 and 0.7, respectively. This demonstrates the expected result that the boundary layer thickness and therefore total pressure distortion content decrease with fan face Mach number. In addition, the losses due to the nacelle shock discussed previously can be seen to increase as Mach number decreases. This is due to the increased diffusion of the flow ahead of the inlet in the pre-compression region, which decreases the amount of flow captured by the inlet and therefore spilled over the nacelle. The increased spillage leads to a higher Mach number around the nacelle and increase shock strength. Therefore, increasing fan face Mach number may also benefit the nacelle design.

The entropy generation in the fan stage due to the loss mechanisms described in Table 4.1 is also shown to increase with fan face Mach number. However, the results of

Figure 4-16 show that there is an optimum fan efficiency for fixed fan geometry, in this case fan diameter and blade trailing edge metal angle. Power balances at a higher fan pressure ratio under the fixed geometric constraint which requires increased rotational speed based on Equations 4.10 and 4.11. Figure 4-17 shows that the fan face Mach number decrease is not sufficient to counteract this increase in fan speed such that there is a minimum relative Mach number. The implication is that fan efficiency may be improved by decreasing the blade trailing edge angle, within operability limits, such that the optimum fan efficiency occurs at a higher fan face Mach number.

Figure 4-18 confirms that increasing fan face Mach number leads to an increase in power savings and that a minimum power required is reached near fan face Mach number of 0.7. Although the minimum is not explicitly demonstrated, after the peak efficiency is reached the decrease in lost propulsive power due to boundary layer thinning are outweighed by the fan performance penalty. The kinetic energy thickness at this point has decreased 4.7% over the cases studied with a corresponding power savings of 12%. However, Figures 4-16 and 4-17 are labeled to show the direction of increased fan airflow and fan stage loading, which shows that increasing fan airflow and decreasing fan pressure ratio increases fan efficiency, within the geometric constraints described above. Therefore, optimizing fan efficiency as described above has a potential to further decrease the overall power required for the integrated propulsion system. Also, recall that the noise audit results in Chapter 2 suggested that decreasing fan pressure ratio may improve overall noise levels.

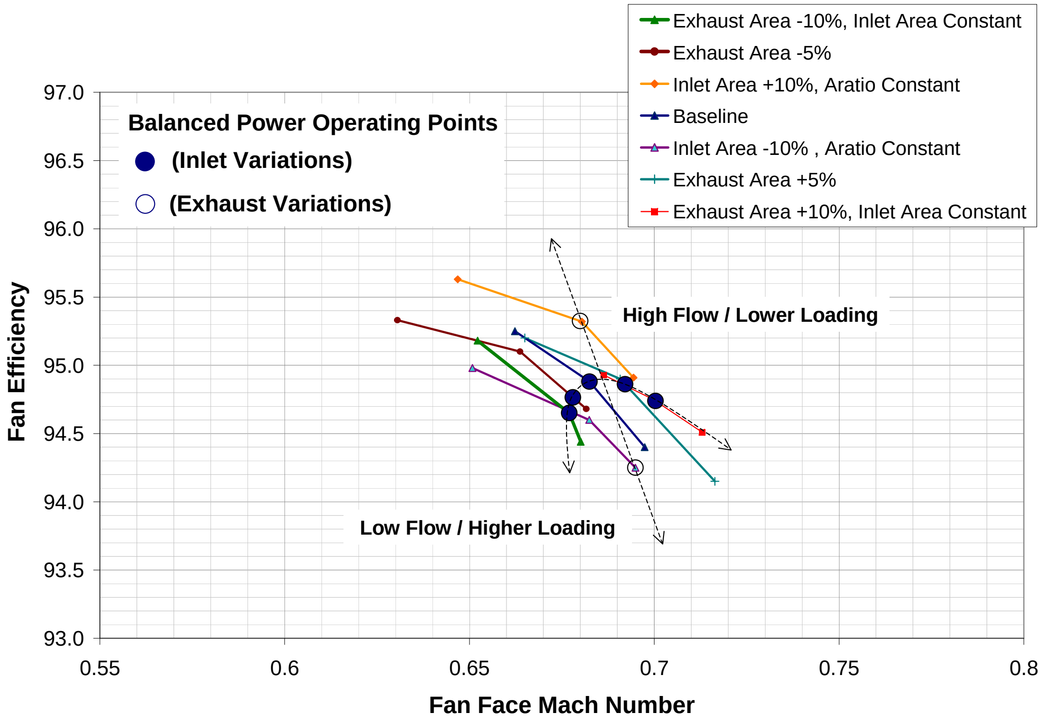

Figure 4-16: Fan efficiency vs. fan face Mach number

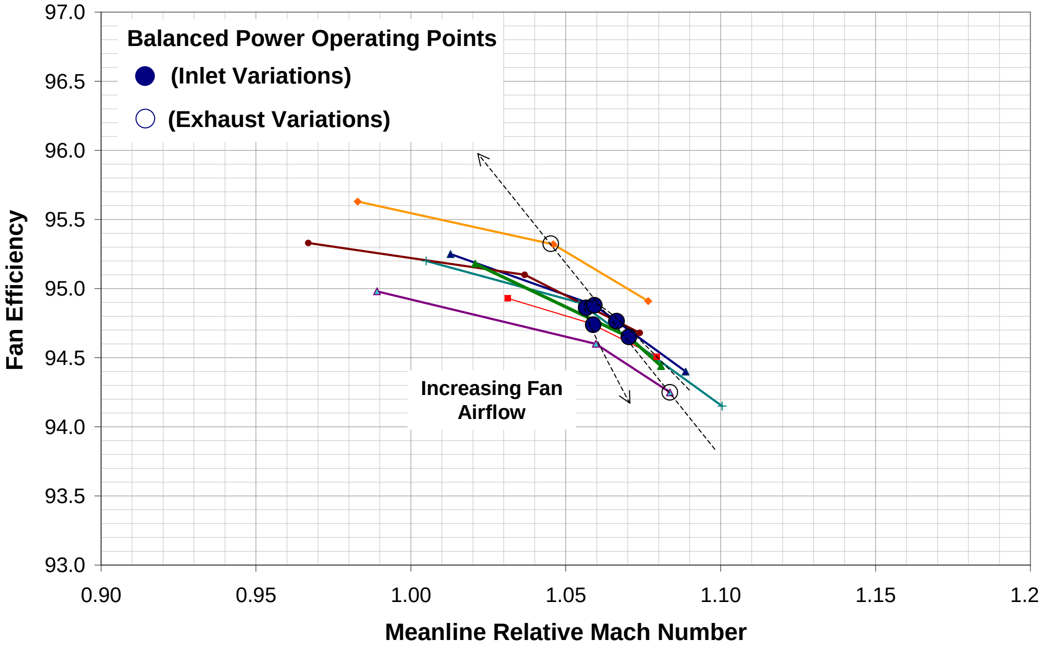

Figure 4-17: Fan efficiency vs. meanline relative Mach number

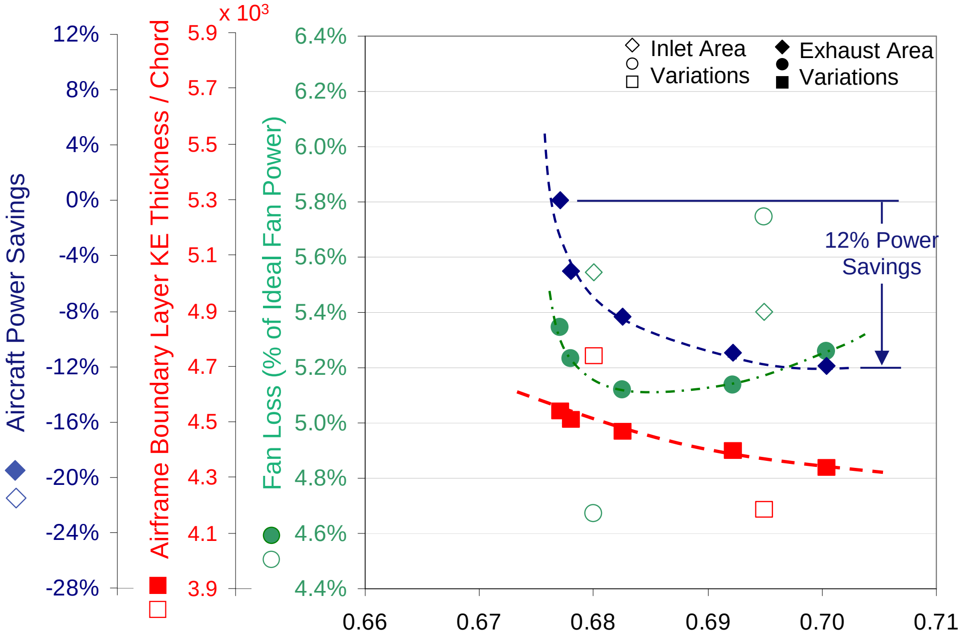

Figure 4-18: Aircraft power savings, airframe boundary layer kinetic energy thickness, and fan efficiency trends

THIS PAGE INTENTIONALLY LEFT BLANK

Chapter 5

Conclusions

5.1 Noise Assessment Summary

Noise generation for the N2A and N2B aircraft has been studied using NASA's Aircraft Noise Prediction Program. Limitations of the program for HWB applications were investigated and specific models were identified for improvement. Based on this analysis, a preliminary FAR 36 certification estimate is made and pre-test predictions were provided for future wind tunnel tests at NASA LaRC 14' by 22' facility.

The key outcomes of the analysis are:

- Improved airfoil self-noise and wingtip models are used consistent with the CMI SAX-40 noise evaluation. The ANOPP noise module relies on empirical data from conventional airframes. Instead, the Ffowcs-Williams and Hall based methodology uses boundary layer properties from a 2-D viscous analysis and calculates the noise amplitude based on first principles.

- The N+2 aircraft do not have the 25% Mach number suppression local to the main landing gear typical of conventional airframes. This results in a 14% increase in peak SPL and makes the main landing gear the loudest noise source on approach.

- The barrier shielding method in ANOPP does not capture the effects of the HWB geometry, as it is based on semi-infinite rectangular barriers. A need for improved acoustic shielding methodology is identified and a diffraction integral method is implemented in a related thesis [4].

- The overall takeoff and landing noise estimates using the model improvements are 5.3 and 26.2[1] EPNdB above the N+2 goal of 52 dB below stage 3 levels for the N2A and N2B, respectively.

- The N2A takeoff noise levels are primarily set by the jet and fan rearward noise where shielding is not as effective. Lowering fan pressure ratio to reduce the exhaust velocity is recommended as a noise mitigation strategy.

- The N2A approach noise can be reduced an additional 4-6 dB with more advanced landing gear fairings as the main landing gear is the peak noise source; however, elevon noise is only 3-4 dB lower and will also need to be improved.

- The N2B noise levels are driven by the propulsion system; however, the acoustic simulation for the N2B propulsion system is found to be inadequate for this analysis. The available tools do not model the distributed propulsion system with rectangular exhaust nozzles.

- Physical constraints on the phased array position for the wind tunnel test will limit the measurement capability to the shielding shadow region. In addition, shielded engine noise is predicted to be more than 20 dB below historic background noise levels, which may be outside DAMAS capability (10-15 dB below background). It is recommended that a no flow test be used such that the microphone array can be positioned forward and aft of the model and eliminate background noise.

- Many of the airframe sources may also be difficult to measure in the wind tunnel test. The landing gear is the loudest at 10-15 dB below background noise levels;

---

[1] Preliminary noise estimate is provided for reference only and will be updated with distributed propulsion system and rectangular exhaust models

however, the elevon noise may be more challenging at more than 30dB below background noise.

5.2 Propulsion System Integration Summary

The impact of increasing fan face Mach number on airframe boundary layer properties and BLI performance trends was also investigated using a 2-D viscous CFD model. A power balance methodology is used to determine the power required by the propulsion system for steady level flight, which also include the outer wing dissipation terms and lift induced drag. Furthermore, a fan actuator volume is included that provides a stagnation temperature and pressure rise to the flow using a body force representation. In this manner, the coupling of the external flow of the airframe and the internal flow of the engine are captured. Empirical and first principles based loss models are used to scale fan losses with local flow relative Mach number.

The key outcomes of the analysis are:

- A fan face Mach number of approximately 0.7 is found to maximize the power savings at 12% relative to the baseline configuration, based on extrapolation of modeled fan loss and airframe boundary layer trends.
- An optimum fan efficiency exists for fixed inlet area and trailing edge metal angle that is at a lower fan face Mach number, 0.68. Power balances at a higher fan pressure ratio under the fixed geometric constraint which requires increased fan speed and the fan face Mach number decrease is not sufficient to reduce the relative Mach number.
- The fan pressure ratio to balance power decreases with increased fan face Mach number which suggests that low pressure ratio high-flow fans are desirable for BLI. The decreased loading will require a lower fan speed and may yield substantive power savings on the aircraft system level.

5.3 Recommendations for Future Work

To reduce the overall engine noise and meet the N+2 goals:

- Fan pressure ratios of 1.4 and 1.5 should be investigated as a means to lower the fan rearward and jet noise sources.
- The noise assessment should be updated based on the diffraction integral shielding methodology described in [4].
- The N2B engine cycle and noise estimates should be updated to more accurately represent the distributed propulsion system configuration with rectangular exhaust nozzles.
- A trade between aircraft weight and noise should be conducted based on the liner length necessary to attenuate the N2B rearward propulsion noise and the liner treatment methodology should be updated in ANOPP.

To further evaluate the N2B propulsion system integration:

- The N2B nacelle should be redesigned with additional 3-D flow relief to minimize shock losses.
- The propulsion system should be integrated in collaboration with Boeing using the SAX-40 S-duct inlet as a baseline, which has already been shaped to maximize total pressure recovery.
- A full 3-D analysis of the airframe and inlet should be carried out to validate the conclusions of the 2-D assessment, as the 2-D body force model only captures the radial inlet flow distortion.
- The distortion transfer through the fan should be characterized using a 3-D body force representation of the fan.
- A Trefftz plane power balance should be conducted using the methodology outlined in Chapter 4.

Bibliography

[1] T. Crabtree, T. Hoang, J. Edgar, and K. Heinicke. (2008) World air cargo forecast: 2008-2009. The Boeing Company. [Online]. Available: http://www.boeing.com/commercial/cargo/wacf.pdf

[2] R. Dahl. (2009, March) Annual twenty-year freighter aircraft forecast: Fourth annual edition 2009 - 2028. Air Cargo Management Group. [Online]. Available: http://www.cargofacts.com/downloads/ACMG%202009%20Freighter%20 Forecast%20Press%20Release.pdf

[3] R. Kawai, "Acoustic prediction methodology and test validation for an efficient low-noise hybrid wing body subsonic transport," Boeing, November 2007, NASA ARMD Subsonic Fixed Wing Project Kick-Off Review, Contract Number NNL07AA54C.

[4] L. W. T. Ng, "Design and acoustic shielding prediction of hybrid wing-body aircraft," Master's thesis, Department of Aeronautics and Astronautics, Cambridge, May 2009.

[5] J. I. Hileman, Z. S. Spakovszky, M. Drela, and M. A. Sargeant, "Airframe design for silent aircraft," in *45th AIAA Aerospace Sciences Meeting and Exhibit.* AIAA Paper 2007-453, January 2007.

[6] E. de la Rosa Blanco, C. A. Hall, and D. Crichton, "Challenges in the silent aircraft engine design," in *45th AIAA Aerospace Sciences Meeting and Exhibit.* AIAA Paper 2007-454, January 2007.

[7] M. Drela and H. Youngren, "Athena vortex lattice," 2006, version 3.26.

[8] M. Drela, "Multi-element airfoil design/analysis software," 2004, version 3.02.

[9] J. I. Hileman, Z. S. Spakovszky, and M. Drela, "Aerodynamic and aeroacoustic three-dimensional design for a silent aircraft," in *44th AIAA Aerospace Sciences Meeting and Exhibit.* AIAA Paper 2006-241, January 2006.

[10] J. Burton, "Propulsion system cycle definitions for the hybrid wing body airplane," NASA Glenn Research Center, ELNHWB Phase I Final Report NNL07AA54C, January 2009.

[11] D. Crichton, E. de la Rosa Blanco, T. R. Law, and J. I. Hileman, "Design and operation for ultra low noise take-off," in *45th AIAA Aerospace Sciences Meeting and Exhibit.* AIAA Paper 2007-456, January 2007.

[12] A. P. Plas, M. A. Sargeant, V. Madani, D. Crichton, E. M. Greitzer, T. P. Hynes, and C. A. Hall, "Performance of a boundary layer ingesting propulsion system," in *45th AIAA Aerospace Sciences Meeting and Exhibit.* AIAA Paper 2007-450, January 2007.

[13] A. Manneville, D. Pilczer, and Z. S. Spakovszky, "Preliminary evaluation of noise reduction approaches for a functionally silent aircraft," *AIAA Journal of Aircraft*, vol. 43, no. 3, pp. 836–840, May 2006.

[14] J. Hileman, "Airfoil self-noise prediction," Internal CMI Silent Aircraft Initiative Report, March 2005.

[15] J. E. Ffowcs-Williams and L. H. Hall, "Aerodynamic sound generation by turbulent flow in the vicinity of a scattering half plane," *Journal of Fluid Mechanics*, vol. 40, no. 4, pp. 657–670, 1970.

[16] D. P. Lockard and G. M. Lilley, "The airframe noise reduction challenge," 2004, NASA TM-2004-213013.

[17] M. Goldstein, *Aeroacoustics.* NY: McGraw-Hill, 1976.

[18] M. R. Fink, "Airframe noise prediction method," FAA-RD-77-29, 1977.

[19] J. Hileman, May 2008, personal communication.

[20] T. F. Brooks and M. A. Marcolini, "Airfoil tip vortex formation noise," *AIAA Journal*, vol. 24, no. 2, pp. 246–252, 1986.

[21] T. F. Brooks, D. S. Pope, and M. A. Marcolini, "Airfoil self-noise and prediction," NASA, Reference Publication 1218, 1989.

[22] J. W. Russel, "Aircraft noise prediction program theoretical manual," NASA, December 2006, Section 8.5.2 – Boeing Airframe Noise Module.

[23] Y. Guo, "A semi-empirical model for aircraft landing gear noise prediction." AIAA Paper 2006-2627, May 2006.

[24] Y. Guo, "Empirical prediction of aircraft landing gear noise," Boeing Phantom Works, CA, July 2005, NASA/CR-2005-213780.

[25] Y. Guo, K. Yamamoto, and R. Stoker, "Experimental study on aircraft landing gear noise," *Journal of Aircraft*, vol. 43, no. 2, pp. 306–317, 2006.

[26] M. G. Smith, B. Fenech, L. C. Chow, N. Molin, W. Dobrzynski, and C. Seror, "Control of noise sources on aircraft landing gear bogies." AIAA Paper 2006-2626, May 2006.

[27] "Aircraft noise prediction program theoretical manual," NASA, July 2004, Section 5.1 – General Suppression Module.

[28] R. Sen, B. Hardy, K. Yamamoto, Y. Guo, and G. Miller, "Airframe noise sub-component definition and model," Boeing Commercial Airplane Company, NASA Contractor Informal Report, January 2000.

[29] R. Sen, B. Hardy, K. Yamamoto, Y. Guo, and G. Miller, "Airframe noise sub-component definition and model," Boeing Commercial Airplane Company, NASA Contractor Report 2004-213255, September 2004.

[30] "Aircraft noise prediction program theoretical manual," NASA, Section 8.5.1 – Airframe Noise Module, TM-83199.

[31] A. Agarwal, A. P. Dowling, H.-C. Shin, W. Graham, and S. Sefi, "A ray tracing approach to calculate acoustic shielding by the silent aircraft airframe," in *12th AIAA/CEAS Aeroacoustics Conference.* AIAA Paper 2006-2618, May 2006.

[32] D. Weir and L. Lieber, "Aircraft noise prediction program theoretical manual," NASA, February 2008, Section 5.3 – Wing Module.

[33] L. L. Beranek, *Noise and Vibration Control.* NY: McGraw-Hill, 1971, pp. 174–180.

[34] Z. Maekawa, "Noise reduction by screens," in *Applied Acoustics.* Elsevier Publishing Company Ltd., 1968, pp. 157–173.

[35] D. Papamoschou, C. Huang, and S. Mayoral, "Uci phase i report," University of California Irvine, ELNHWB Phase I Final Report - Appendix B NNL07AA54C, October 2008.

[36] W. Dobrzynksi, L. Chow, C. Wood, M. Smith, and C. Seror, "Design and testing of low noise landing gears," in *11th AIAA/CEAS Aeroacoustics Conference.* AIAA Paper 2005-3008, May 2005.

[37] T. Law and A. Dowling, "Optimization of annular and cylindrical liners for mixed exhaust aeroengines," in *13th AIAA/CEAS Aeroacoustics Conference.* AIAA Paper 2007-3546, May 2007.

[38] T. Brooks, "Hybrid Wing Body Acoustic Test Program – Test Plan," 2008.

[39] T. Brooks and W. Humphreys, Jr., "A deconvolution approach for the mapping of acoustic sources (DAMAS) determined from phased microphone arrays," *Journal of Sound and Vibration*, vol. 294, no. 4–5, pp. 856–879, July 2006.

[40] W. Humphreys, Jr. and T. F. Brooks, "Noise spectra and directivity for a scale-model landing gear," in *13th AIAA/CEAS Aeroacoustics Conference.* AIAA Paper 2007-3458, May 2007.

[41] D. Halliday, R. Resnick, and J. Walker, *Fundamentals of Physics*, 5th ed. New York, NY: John Wiley and Sons Inc., 1997.

[42] P. Soderman and C. Allen, *Aeroacoustic Measurements.* Germany: Springer, 2002, ch. Microphone Measurement In and Out of Airstream, pp. 34–53.

[43] F. Hutcheson, “Noise tests in the 14 x 22 facility,” boeing NRA Kickoff Meeting, Nov. 5th 2007.

[44] D. D. Mobed, “Experimental aero-acoustic assessment of swirling flows for drag applications,” Master’s thesis, Department of Aeronautics and Astronautics, Cambridge, May 2007.

[45] R. H. Schlinker and J. C. Simonich, “Acoustic test planning,” February 2010, NASA ELNHWB meeting.

[46] M. Drela, “Power balance in aerodynamic flows,” *AIAA Journal*, vol. 47, no. 7, pp. 1761–1771, 2009.

[47] M. B. Giles and R. M. Cummings, “Wake integration for three-dimensional flowfield computations: Theoretical development,” *Journal of Aircraft*, vol. 36, no. 2, pp. 357–365, 1999.

[48] L. H. Smith, Jr., “Wake ingestion propulsion benefit,” *Journal of Propulsion and Power*, vol. 9, no. 1, pp. 74–82, 1993.

[49] M. A. Sargeant, “Boundary layer ingestion for advanced airframes,” Ph.D. dissertation, Department of Engineering, December 2007.

[50] *FLUENT 6.3 Users Guide*, Fluent Inc., Lebenon, NH, 2006.

[51] D. Crichton, “Fan design and operation for ultra low noise,” Ph.D. dissertation, Department of Engineering, 2007.

[52] J. D. Denton, “The 1993 igti scholar lecture: Loss mechanisms in turbomachinery,” *Journal of Turbomachinery*, vol. 115, no. 4, pp. 621–656, 1993.

[53] D. Hall, NASA N+3 Project, 2009, personal communication.

[54] C. Reid, “The response of axial flow compressors to intake flow distortions,” no. 69-GT-29, 1969.

[55] E. M. Greitzer, C. S. Tan, and M. B. Graf, *Internal Flow: Concepts and Applications.* Cambridge, UK: Cambridge University Press, 2004.

[56] H. Schlichting, *Boundary Layer Theory*, 7th ed. New York, NY: McGraw-Hill, 1979.